

MISS KAROLINA KOŚMIŃSKA (Orcid ID : 0000-0001-8775-9885)

DR. JAROSLAW MAJKA (Orcid ID : 0000-0002-6792-6866)

Article type : Original Article

Deciphering late Devonian-early Carboniferous P-T-t path of mylonitised garnet-mica schists from Prins Karls Forland, Svalbard

Karolina Kościńska¹, Frank S. Spear², Jarosław Majka^{1,3}, Karol Faehnrich⁴, Maciej Manecki¹, Karsten Piepjohn⁵, Winfried K. Dallmann⁶

¹*Faculty of Geology, Geophysics and Environmental Protection, AGH University of Science and Technology, al. Mickiewicza 30, 30-059 Kraków, Poland*

²*Department of Earth and Environmental Sciences, Rensselaer Polytechnic Institute, 110 8th Street, Troy, NY 12180, USA*

³*Department of Earth Sciences, Uppsala University, Villavägen 16, 752-36 Uppsala, Sweden*

⁴*Department of Earth Sciences, Dartmouth College, HB 6105 Fairchild Hall, Hanover, NH 03755, USA*

⁵*Federal Institute for Geosciences and Natural Resources (BGR), Stilleweg 2, 30655 Hannover, Germany*

⁶*Institute of Geosciences, UiT The Arctic University of Norway, P.O.Box 5060 Langnes, 9037 Tromsø, Norway*

Corresponding author: karolina.kosminska@agh.edu.pl

SHORT TITLE: Ellesmerian metamorphism in Svalbard

This article has been accepted for publication and undergone full peer review but has not been through the copyediting, typesetting, pagination and proofreading process, which may lead to differences between this version and the [Version of Record](#). Please cite this article as [doi: 10.1111/JMG.12529](https://doi.org/10.1111/JMG.12529)

This article is protected by copyright. All rights reserved

ABSTRACT

Quartz-in-garnet inclusion barometry integrated with trace element thermometry and calculated phase relations is applied to mylonitised schists of the Pinkie unit cropping out on the island of Prins Karls Forland (PKF), western part of the Svalbard Archipelago. This approach combines conventional and novel techniques and allows deciphering the P-T evolution of mylonitic rocks, for which the pressure-temperature conditions could not have been easily deciphered using traditional methods. The results obtained suggest that rocks of the Pinkie unit were metamorphosed under amphibolite facies conditions at 8-10 kbar and 560-630°C and mylonitised at ~ 500-550 °C and 9-11 kbar. The P-T results are coupled with *in-situ* Th-U-total Pb monazite dating, which record amphibolite-facies metamorphism at c. 359-355 Ma. This is the very first evidence of late Devonian-early Carboniferous metamorphism in Svalbard and it implies that the Ellesmerian Orogeny on Svalbard was associated with metamorphism up to amphibolite facies conditions. Thus, it can be concluded that the Ellesmerian collision between the Franklinian margin of Laurentia and Pearya and Svalbard caused not only commonly accepted brittle deformation and weak greenschist facies metamorphism, but also a burial and deformation of rock complexes at much greater depths at elevated temperatures.

Key words: QuiG barometry, monazite, Ellesmerian Orogeny, High Arctic, Pinkie unit, Svalbard

1 INTRODUCTION

Petrologic and geochronologic studies of mylonites provide a means for determination of the pressure-temperature (P-T) conditions and timing of formation of shear zones. Understanding the formation of mylonites is important for our reasoning about large-scale tectonic processes. Towards this end, considerable effort has been spent in the study of brittle and ductile shear zones in the relatively poorly understood region of the High Arctic (e.g. Mazur et al., 2009; Colpron & Nelson,

2011; McClelland et al., 2012; Braathen, Osmundsen, Maher, & Ganerød, 2018). Southwestern Svalbard is an especially important terrane in the High Arctic, bearing a record of at least five orogenic events (e.g. Majka & Kościńska, 2017) and having still unresolved paleogeographic affinity. Therefore, an in-depth study of any large-scale shear zone and associated mylonitic rocks in this region substantially broadens our knowledge about the geological evolution of the High Arctic and the North Atlantic region. One such shear zone is the Eocene Bouréefjellet Fault Zone exposed in westernmost Svalbard, which is hypothesized to deform already sheared Ellesmerian metamorphic amphibolite-facies rocks (Schneider, Faehnrich, Majka, & Manecki, 2019).

The goal of the present study is to constrain the pressure-temperature-time (P–T–t) conditions of metamorphism and mylonitization of rocks from the Pinkie unit through a combination of thermobarometric techniques and dating of accessory phases. Mylonites such as those exposed within the aforementioned fault zone commonly preserve mineral assemblages that could be out of equilibrium, which results from recrystallization of already existing mineral phases and the formation of new ones, usually in presence of fluids. In this study, we have applied a combination of thermobarometric methods to attempt to unravel the complex P–T history including: inclusion elastic thermobarometry (Enami, Nishtyama, & Mouri, 2007; Kohn, 2014; Ashley, Caddick, Steele-MacInnis, Bodnar, & Dragovic, 2014; Angel, Mazzucchelli, Alvaro, Nimis, & Nestola, 2014; Thomas & Spear, 2018), trace element thermometry (Pyle et al. (2001)), and calculated phase equilibria using the method of differential thermodynamics (i.e. Spear, 1993). Moreover, we report the results of *in-situ* Th-U-total Pb monazite dating that, coupled with the P-T data, provide the first record of the amphibolite facies Ellesmerian metamorphism on Svalbard and in the High Arctic in general. The latter bears significant importance for construction and interpretations of paleogeographic models for this part of the world and provides the first direct link between Paleozoic European and Canadian segments of the High Arctic.

2 GEOLOGICAL SETTING

2.1 Ellesmerian Orogeny in the High Arctic

The northern margin of North America and the western margin of the Barents Shelf bear evidence of an up to 400 km wide Devonian-Carboniferous (Ellesmerian) fold-and-thrust belt, which is exposed

from the western Canadian Arctic Islands and North Greenland towards Svalbard over a length of more than 3000 km (e.g., Piepjohn, von Gosen, Läufer, McClelland, & Estrada, 2013, Piepjohn et al., 2015 and references therein, Figure 1). This fold-and-thrust belt is the result of the Ellesmerian Orogeny, which took place after the main stages of the Caledonian Orogeny on the Pearya terrane of northern Ellesmere Island and Svalbard and after the formation of the post-Caledonian Old Red Sandstone molasse basins in Svalbard (e.g., Vogt 1936; Harland, 1997; Piepjohn, 2000; Dallmann, 2015). The Ellesmerian fold-and-thrust belt is generally characterized by brittle deformation and thrusting with locally pronounced greenschist-facies metamorphism documented on Ellesmere Island (Klaper, 1990, 1992; Klaper & Ohta, 1992; Piepjohn, von Gosen, Tessensohn, & Saalman, 2008) and in North Greenland (Dawes, 1971; Dawes & Soper, 1973; Soper & Higgins, 1991). The timing of the Ellesmerian Orogeny is not well constrained. The time frames for this event were set based on the observations from three localities: the Parry Islands, where the Ellesmerian deformation is thought to be younger than strata of Famennian and early Late Carboniferous ages (Harrison, Fox, & Okulitch, 1991), the northernmost Devon Island, where Viséan sediments unconformably overly deformed Late Frasnian to Early Famennian deposits of the Parry Islands Formation indicating the latest Devonian to earliest Carboniferous age for the Ellesmerian deformation (Mayr, de Freitas, Beauchamp, & Eisbacher, 1998), and Svalbard, where palynological observations in deformed latest Famennian Old Red Sandstone deposits and unconformably overlying Viséan sediments indicate an even shorter time span within the Tournaisian for the Ellesmerian (locally called Svalbardian) deformation (Piepjohn, Brinkmann, Grewing, & Kerp 2000; Piepjohn & Dallmann, 2014). The Ellesmerian Orogeny has affected Neoproterozoic to Devonian sediments of the Franklinian Basin in the Canadian Arctic and North Greenland (e.g., Thorsteinsson & Tozer, 1970; Soper & Higgins, 1991; Trettin, 1991a) and was related to the approach and docking of the Pearya Terrane and Svalbard to the northern margin of Laurentia (Trettin, 1991b; Klaper, 1990, 1992; Klaper & Ohta, 1992; Bjørnerud & Bradley, 1994; Piepjohn et al., 2013, 2015).

2.2 Ellesmerian Orogeny in Svalbard

The Ellesmerian Orogeny on Svalbard is dominated by west-directed folding and thrusting (e.g., Friend, 1961; Friend, Heintz, & Moody-Stuart, 1966; Gee & Moody-Stuart, 1966; Harland, 1997)

concentrated within several N-S trending deformation zones (Piepjohn, 2000). The Ellesmerian deformation has mainly affected the Old Red Sandstone Basin in northeastern Spitsbergen and on Sørkapp Land in the south (Holtedahl, 1914; Vogt, 1938; Orvin, 1940; Friend, 1961; Birkenmajer, 1964; Gee & Moody-Stuart, 1966; Murašov & Mokin, 1979; Dallmann, 1992; Dallmann et al., 1993; Piepjohn, 2000; Piepjohn & Dallmann, 2014). The Caledonian basement of Svalbard north of Kongsfjorden (Brøggerhalvøya) and south of the St. Jonsfjorden (Figure 2a) was also partly involved in the Ellesmerian Orogeny (Thiedig & Manby, 1992; Piepjohn, et al., 1997; Piepjohn, 2000; Tessensohn, von Gosen, & Piepjohn, 2001; Barnes, Walczak, Janots, Schneider & Majka, 2020).

2.3 The Pinkie unit on Prins Karls Forland

Prins Karls Forland is a narrow, 80 km long island off the west coast of Spitsbergen island (Figure 2a). It is separated from the latter by the N-S trending Paleogene Forlandsundet Graben and consists of a heterogeneous succession of Neoproterozoic (to possibly Early Paleozoic) metamorphosed rocks which are difficult to correlate with the Caledonian basement sequences on the main land of Spitsbergen. The Pinkie unit of PKF crops out in a very limited area in the vicinity of Grimaldibukta (Figure 2b). It represents the highest grade (amphibolite-facies) metamorphic rocks on PKF (*e.g.* Hjelle et al., 1999; Manby, 1986). The Pinkie unit occurs in high mountains that are surrounded by steep, crevassed glaciers (Figure 3a). Therefore, the number of available outcrops is limited and hard to access. The Pinkie unit is overthrust by the greenschist facies Grampianfjellet Group in the west and it is in normal-fault contact with the Scotiafjellet Group in the east (Figure 2b). The type locality for the Pinkie unit is the mountain Bouréefjellet, where the most complete succession is exposed (Figures 2b, 3a). Along the NE-slope of Bouréefjellet, the Pinkie unit consists mainly of mylonitised, laminated quartzites and garnet-bearing mylonitised metapelites (Figure 3b). The lowermost part of the section comprises quartzites with laminae enriched in carbonates. Up section, carbonate laminae disappear and the rock becomes a pure quartzite. Even higher up section, mylonitic, garnet-bearing metapelites predominate and continue to the uppermost parts of the profile.

The ages of the Pinkie unit and the surrounding rocks are poorly constrained. Preliminary detrital zircon dating of a quartzite sample from the section described above yielded U-Pb ages as young as *c.* 950 Ma (Kośmińska et al., 2015). The surrounding Grampianfjellet and Scotiafjellet groups are thought to be of Neoproterozoic to possibly Early Paleozoic depositional age (*e.g.* Hjelle, Ohta, &

Winsnes, 1979; Hjelle et al., 1999; Knoll 1992). Deformation and metamorphism of the pre-Devonian rock units on PKF have been traditionally interpreted as being solely Caledonian in age (e.g., Harland, Horsfield, Manby, & Morris, 1979; Manby, 1986). The Pinkie unit rocks are overprinted by younger Eocene (Eurekan) deformation, a timing of which has recently been derived by Schneider et al. (2019) who dated white mica in the thrust zone overlying the Pinkie unit. This ^{40}Ar - ^{39}Ar white mica dating yielded the age of deformation to be *c.* 54-44 Ma. Some of the single crystals of mica have preserved evidence of an earlier deformation event at *c.* 320 Ma, thus possibly Ellesmerian.

2.4 Structural framework

The metasediments of the Pinkie unit are deformed in a brittle to ductile fault zone comprised of mylonites, phyllonites, and cataclasites with brittle deformation dominating towards the upper contact with the Grampianfjellet Group and ductile deformation dominating in the lower structural levels (Schneider et al., 2019). The strong Eocene overprint hinders observations of the Ellesmerian fabric.

Measurements of lineations throughout the area of study display a scattered pattern, with two dominating directions, gently plunging to the north and to the south (Figure 2c). A stretching lineation is present and is mostly defined by elongated aggregates of quartz, mica and feldspar. Crenulations were also observed in the field, following a similar N-S direction as the stretching lineations. Asymmetric clasts of quartz in mylonites and metasediments, as well as a C-S fabric, indicate top to the north directions.

3 ANALYTICAL METHODS

3.1 Electron microprobe analyses and X-ray maps

The X-ray maps of the garnet (except for the map in Figure 7) and monazite grains, step profiles and point analyses were collected using a Jeol SuperProbe JXA-8230 electron microprobe at the AGH University of Science and Technology, Kraków, Poland. The analytical conditions were as follows: for monazite maps, an accelerating voltage of 15 kV, a beam current of 100 nA, a dwell time of 50 ms, and 0.1 - 0.3 μm step size was used; for garnet maps, an accelerating voltage of 15 kV, a beam current of 100 nA, a dwell time of 50 ms and 0.5 μm step size was used; and point analyses were made using an accelerating voltage 15 kV, 20 nA beam current, counting times of 10 s on peaks and 5 s on \pm background positions with a focused beam. Only the $\text{K}\alpha$ lines were measured. Synthetic and

natural standards were used for calibration. The raw data were reduced and corrected using the PRZ routine. Additional garnet X-ray maps were performed on the Cameca SX-100 microprobe at Rensselaer Polytechnic Institute and collected using an accelerating voltage of 15 kV, a 100 nA beam current, a dwell time of 50 ms and 0.5 μm step size.

3.2 QuiG barometry

Quartz-in-garnet (QuiG) barometry allows determination of the pressure of entrapment of a quartz inclusion in garnet, and hence the pressure at which garnet overgrew the quartz by using the pressure effect of the Raman shift of the inclusion (Enami, Nishtyama & Mouri, 2007; Kohn, 2014; Thomas & Spear, 2018 and references therein). Raman spectra were collected at Rensselaer Polytechnic Institute using a Bruker Senterra Raman Spectrometer coupled with an Olympus CX51 microscope. Measurements were performed using a 532 nm laser, 1200 grooves/mm grating and four co-additions of 10 seconds each. This Raman instrument is self-calibrating, however Herkimer quartz and quartz from the matrix were measured at the beginning and end of the Raman session and used as the reference material against which to calculate the Raman shift of the inclusions. Only the 464 cm^{-1} peak was measured and the uncertainty of the Raman shift of this peak was determined to be on the order of $\pm 0.1\text{ cm}^{-1}$ as verified by repeated analysis of standard materials.

The internal pressure of quartz inclusions at ambient temperature was calculated from the Raman shift using the calibration of Schmidt & Ziemann (2000). The thermoelastic model of Guiard & Powell (2006) with correction and parameters proposed by Angel, Alvaro, Miletich & Nestola (2017a) and Angel, Mazzucchelli, Alvaro & Nestola (2017b) were used to calculate isomekes of inclusion entrapment. Thomas & Spear (2018) have verified experimentally that QuiG barometry is capable of recovering the pressure of entrapment to an overall accuracy of better than 10%. The precision of QuiG barometry, which is important for comparing results from different samples, was inferred by Kohn (2014) and Thomas & Spear (2018) to be on the order of ± 300 bars.

3.3 Electron microprobe monazite dating and trace elements analyses

In-situ Th–U–total Pb dating of monazite was performed using a Cameca SX-100 electron microprobe at the Department of Electron Microanalysis at the Dionýz Štúr State Geological Institute (Geological Survey) in Bratislava, Slovak Republic. Monazite was analyzed using a 180 nA beam current and 15

kV accelerating potential with a beam diameter of 1 to 3 μm , with counting times for Pb=150 s, Th=45 s, U=75 s, Y=45 s and for all other elements 25–35 s. The following standards were used for calibration: phosphates XPO₄ for REE and Y, ThO₂ for Th, galena for Pb, UO₂ for U, wollastonite for Ca and Si, and Al₂O₃ for Al. Data handling and individual spot-age determinations were made using DAMON software (P. Konečný, unpublished) following the chemical total-Pb age equation of Montel, Foret, Veschambre, Nicollet & Provost (1996). ISOPLOT software (Ludwig, 2001) was used for the weighted-mean age and 2σ uncertainty (95% confidence level) calculations. More details concerning the monazite dating method are presented in Petrik & Konečný (2009) and Konečný, Kusiak and Dunkley (2018).

3.4 Thermodynamic calculations

Pressure-temperature diagrams were contoured for garnet composition and amount using the method of differential thermodynamics in program Gibbs (Spear, 1988; Spear and Menard, 1989; Spear, 1993) using the internally consistent SPaC (Spear, Pattison, Cheney) dataset (Spear and Pyle, 2010), which is based on Berman (1988). The method of differential thermodynamics was used because it does not require enthalpy data (only entropies, volumes, and activity models are required) and, most importantly, it is designed to calculate *changes* in mineral composition and amounts and is thus well-suited for the analysis of rocks in which the effective bulk composition is not well-constrained or may change as the P–T conditions evolve. In this study, the initial bulk rock compositions for each sample were computed from the major mineral modes and compositions and calculations were made relative to a reference P–T point that was inferred to be the peak metamorphic conditions for the sample.

4 PETROLOGICAL DESCRIPTION

4.1 Petrography and textures

Several rock samples were collected from the Pinkie unit and petrographic analysis was carried out on 47 thin sections. Microscopic observations revealed three different garnet-bearing assemblages within the Pinkie metapelites: (1) garnet-staurolite-muscovite-biotite-plagioclase-quartz, (2) garnet-staurolite-kyanite-muscovite-biotite-plagioclase-quartz and (3) garnet-kyanite-muscovite-biotite-plagioclase-quartz. Three representative thin sections have been chosen for further petrological studies and for monazite dating (see Figures 2b, 3a and Table 1 for samples location, mineral assemblages and GPS coordinates). A description of the metapelites used in this study is presented

below and microphotographs are shown on the Figure 4. The mineral abbreviation for sericite is Se and the other abbreviations are after Kretz (1983).

Petrographic observations reveal that the Pinkie rocks experienced two main deformational events. The S1 foliation is defined by biotite and muscovite which formed during amphibolite-facies metamorphism. Two generations of garnet are present. Garnet-I (Grt-I) forms large porphyroblasts, up to 3 mm in diameter (Figure 4a, b, c, f), is strongly deformed, commonly elongated, and has rims that locally show evidence for resorption (Figure 4b, f). Grt-I contains inclusions of quartz, ilmenite, apatite, tourmaline, zircon and monazite. Some of the quartz inclusion trails indicate pre-Grt-I alignment of grains, (Figure 4a) and indicate rather static growth of the garnet. Staurolite overgrows Grt-I (Figure 4a, b) or forms separate porphyroblasts (Figure 4d) and contains numerous quartz and ilmenite inclusions. Staurolite is locally replaced by sericite filling cracks. Kyanite forms elongated, strongly deformed aggregates that are aligned within the foliation (Figure 4d, e, f). Locally, it is partially replaced by fine-grained sericite (Figure 4g). Plagioclase forms porphyroblasts in the matrix and biotite and muscovite are predominant matrix phases (Figure 4b-e). Tourmaline is abundant both in the matrix and as inclusions in Grt-I. Ilmenite occurs as inclusions within Grt-I and staurolite and as elongated single grains in the matrix.

Metamorphic assemblages and S1 textures are strongly overprinted by S2 mylonitisation (Figure 4a-h). The mylonitic fabric (commonly parallel to S1) obliterates the S1 foliation, greatly reducing the grain size in distinct bands. It is underlined by newly formed ribbon-like quartz layers and wraps around Grt-I, staurolite and plagioclase porphyroblasts and is responsible for fracturing of these porphyroblasts.

Garnet-II (Grt-II) occurs as small (< 0.5mm diameter), idioblastic crystals (Figure 4h) or as overgrowths on the outermost rims of Grt-I. The lack of deformation associated with Grt-II suggests it is of late syn-mylonitic origin.

4.2 Mineral chemistry

Three representative thin sections (KK14-35, KK12-5b and KK14-33) have been studied in detail including microprobe X-ray mapping and spot analyses. Representative analyses of garnet are listed in Table 2 and of muscovite, biotite and staurolite in Table 3. The description of the chemistry of major minerals is presented below.

Sample KK14-35

Grt-I shows distinct chemical zoning between core and rim (Figure 5). Its composition varies from $\text{Alm}_{82}\text{Grs}_4\text{Prp}_{12}\text{Sps}_2$ in the core to $\text{Alm}_{80}\text{Grs}_8\text{Prp}_{10}\text{Sps}_2$ in the rim (Figure 6). Spessartine shows a complex pattern. Generally, it decreases from the core to the rim, and then increases in the outermost rim (Figure 6). However, the X-ray maps reveal several discrete internal domains enriched in Mn (Figure 5). The difference in spessartine values between such domains is very small (less than 0.01 Sps). Almandine slightly increases from core to the rim, whereas pyrope generally decreases except the outermost rim, where it increases again. Grossular shows even distribution in the core, but it rises towards the rim before increasing in the outermost rim. Grt-II overgrows Grt-I (Figures 5, 6, 7) or forms single, small, idioblastic grains. Grt-II is easily recognizable on the X-ray maps by the higher grossular and lower almandine rims on Grt-I (Figure 5, 7). Grt-II overgrowing Grt-I shows an average composition of $\text{Alm}_{80}\text{Grs}_{11}\text{Prp}_8\text{Sps}_1$. Only slight zoning has been observed in individual Grt-II crystals (Figure 7) and it is generally characterized by flat profiles of almandine (0.80-0.83), pyrope (0.10-0.13), low spessartine (<0.1), and grossular decreasing from the core (0.09) to the rim (0.05). Staurolite is characterized by $X_{\text{Fe}} = \text{Fe}/(\text{Fe}+\text{Mg})$ of 0.78-0.83 with higher values near the contact with garnet. ZnO content is low, reaching up to 0.32 wt.%. Muscovite contains Si of 3.07-3.11 apfu. The X_{Fe} in biotite ranges between 0.45 and 0.52 and biotite is characterized by low Ti content up to 0.06 apfu. Plagioclase composition is nearly uniform across the grains and has a composition of $\text{Ab}_{90}\text{An}_9\text{Or}_1$.

KK12-5b

Grt-I shows similar zoning as the Grt-I in sample KK14-35. Its composition varies from $\text{Alm}_{88}\text{Grs}_2\text{Prp}_8\text{Sps}_2$ in the core to $\text{Alm}_{89}\text{Grs}_2\text{Prp}_8\text{Sps}_1$ in the rim (Figure 6). Almandine, pyrope and grossular vary slightly, whereas spessartine decreases towards the rim. Grt-I is penetratively fractured. The majority of fractures are filled by late chlorite, which could be a reason for scattering of almandine and pyrope on the profiles (Figure 6). The composition of Grt-II is $\text{Alm}_{80}\text{Grs}_9\text{Prp}_{10}\text{Sps}_1$. The grossular zonation is defined by discrete core and rim domains with low grossular cores in sharp contact with high grossular rims (Figure 5). Staurolite porphyroblasts have $X_{\text{Fe}} = 0.84-0.86$ with higher values towards the rim. The maximum ZnO content is 0.71 wt %. Muscovite is characterized

by Si varying from 3.04 to 3.14 apfu. Biotite has X_{Fe} of 0.52-0.58 and Ti ranging from 0.06 to 0.12 apfu. Plagioclase is mostly albitic, with composition $\text{Ab}_{90}\text{An}_{10}\text{Or}_0$.

KK14-33

Grt-I displays a similar zoning pattern as the equivalent garnet generations in other samples. It varies from $\text{Alm}_{77}\text{Grs}_4\text{Prp}_{11}\text{Sps}_8$ in the core to $\text{Alm}_{83}\text{Grs}_4\text{Prp}_9\text{Sps}_4$ in the rim. Spessartine shows a bell-shaped profile (Figures 5, 6). Almandine slightly increases on the rims. Pyrope and grossular exhibit rather flat profiles. Similar to sample KK12-5b, the almandine and pyrope trends are scattered. Grt-II commonly overgrows Grt-I with a composition of $\text{Alm}_{77}\text{Grs}_{11}\text{Prp}_{11}\text{Sps}_1$. These discontinuous, relatively grossular-enriched and spessartine- and almandine-depleted overgrowths are easily visible on the X-ray maps (Figure 5; see upper right part of the garnet porphyroblast). Idioblastic grains of Grt-II are sporadically encountered in the matrix. Muscovite contains Si between 3.07 and 3.13 apfu; biotite has X_{Fe} ranging from 0.54 to 0.60 and Ti content from 0.10 to 0.16 apfu. Plagioclase has higher anorthite component than in the samples KK14-35 and KK12-5b ($\text{Ab}_{75}\text{An}_{24}\text{Or}_1$)

4.3 Accessory phases

Accessory phases are represented by monazite, xenotime, allanite, fluorapatite, ilmenite, and zircon. Monazite is present in the matrix and also as inclusions in garnet and/or staurolite. Commonly, it occurs as small, anhedral grains (10-30 μm) but rarely it forms larger grains up to 50 μm in length (Figure 8). Some of the matrix monazite grains are surrounded by reaction coronas that are composed of fluorapatite and allanite (Figure 9). Allanite is present only within these coronas, whereas fluorapatite commonly occurs in the matrix and within garnet and/or staurolite. Tiny (~5-10 μm in diameter) xenotime inclusions have been found in the cores of some of the garnet porphyroblasts although xenotime is absent in the matrix. The metapelites also contain a large number of zircon grains preserved as inclusions in various porphyroblasts as well as in the matrix.

4.4 Monazite chemistry

Representative analyses of monazite are given in the Table 4. X-ray maps show internal concentric, but irregularly shaped zoning of Y, Th and U (Figures 8, 10; Table 4; see also Supporting Information in Table S1). Single monazite grains consist of two or three distinct zones. Monazite-I (Mnz-I) is characterized by high Th ($\text{ThO}_2 > 6.2$ wt.%) and moderate Y ($\text{Y}_2\text{O}_3 = 0.44$ -1.78 wt. %) and forms cores of some of the grains examined (Figure 8a, c). The second population, monazite-II (Mnz-II), is

characterized by high Y content (up to 2.32 wt.%) and ThO₂ contents between 2.25 and 5.82 wt.%. Monazite-II overgrows discontinuously Mnz-I (Figure 8a, c, d) or forms cores of grains (Figure 8b). The third type, monazite-III (Mnz-III), contains lower Y (Y₂O₃ = 0.11-0.96 wt.%) and moderate Th, similar to those encountered in Mnz-II (ThO₂ = 1.83-5.76 %). This Y-depleted population forms thin rims on Mnz-II (Figure 8a, b, c). Mnz-III has never been observed in contact with Mnz-I. Most of the matrix monazites contain Mnz-III, but only Mnz-I and Mnz-II are found as inclusions in Grt-I.

5 P-T ESTIMATES

The Pinkie unit metapelites experienced a complex tectono-metamorphic history accompanied by pervasive deformation. The textures as well as garnet compositional maps show that chemical equilibrium between minerals may not have been achieved throughout the entire history of each sample, due to severe deformation and complex metamorphic evolution of the rocks. Nevertheless, QuiG barometry should provide an estimate of the pressure of garnet formation and yttrium in monazite trace-element thermometry should provide an estimate of the temperature of monazite formation. Additionally, the differential thermodynamic approach should provide at least semi-quantitative constraint on the P–T path between the formation of Grt-I (i.e. the initial, peak metamorphism conditions) and Grt-II (i.e. the conditions just subsequent to mylonitization).

5.1 Quartz-in-garnet (QuiG) Raman barometry

More than 60 quartz inclusions within garnets (both Grt-I and Grt-II) from the samples KK14-35, KK12-5b and KK14-33 were analyzed. The inclusions chosen for the Raman measurements were 5 to 30 μm in diameter. Measured inclusions were located below the surface, far from fractures and other inclusions (see Kohn, 2014, and Thomas & Spear, 2018, for more details of the methodology).

The measured quartz inclusions did not show significant variations in Raman shifts depending on the position within garnet, suggesting that garnet grew under nearly constant P–T conditions (see also Wolfe and Spear, 2018, for a discussion of samples with similar results). Because it is relatively easy for included quartz grains to experience a decrease in the pressure on the inclusion due to the formation of nearby fractures, the maximum shift was chosen as that representative of garnet formation. This choice is substantiated by the experimental study of Thomas and Spear (2018). The maximum observed shift of the 464 cm⁻¹ band of quartz in Grt-I equals 1.05 cm⁻¹ in sample KK14-35,

1.80 cm^{-1} in KK12-5b, and 2.10 cm^{-1} in KK14-33, respectively (Figure 11a). The highest shift obtained for quartz inclusions in Grt-II was 2.70 cm^{-1} . The calculated isomekes from the maximum Raman shifts are plotted on Figure 11b. At a nominal temperature of 550 °C, the isomekes indicate entrapment pressures of 8 – 9.5 kb for Grt-I in the three samples and close to 11 kb for Grt-II.

5.2 Yttrium in monazite thermometry

The Y-in-monazite thermometer based on the calibration of Pyle et al. (2001) has been used to obtain the temperature of monazite formation. The xenotime inclusions within Grt-I cores confirm the presence of xenotime during early stages of metamorphism. Moreover, Grt-I cores exhibit the highest Y values (Figure 12) with Y decreasing towards the rims, whereas the outermost tiny rims show the opposite trend (increasing Y). The general decrease of Y in Grt-I from the core to the rim suggests xenotime breakdown and monazite crystallization. The temperatures for Mnz-II preserved as inclusions in Grt-I have been calculated to be 557 °C, 595 °C, and 629 °C for samples KK14-35, KK12-5b, and KK14-33, respectively, as shown by the vertical dashed lines in Figure 11. Inasmuch as these monazites are included in garnet, these represent minimum temperatures for garnet formation.

5.3 Calculated phase relations

Calculation of garnet compositional isopleths and molar amounts using the differential thermodynamic method described above show similar trends for all three samples, so only the results for the staurolite-bearing sample KK14-35, containing significant amount of Grt-II, are presented here.

The initial modal concentrations of quartz (0.3), garnet (0.02), muscovite (0.3), biotite (0.07), plagioclase (0.2), chlorite (0.1) and staurolite (0.01) and their compositions (Table 2 and Table 3) have been assumed at a reference point of 555°C and 7.5 kbar as indicated by the intersection of QuiG barometry and monazite thermometry (reference point shown as a star on Figure 13). Isopleths of spessartine, grossular and X_{Fe} for Grt-I are presented as solid lines, whereas isopleths corresponding to the compositions of Grt-II are shown as a dotted lines (Fig 13). As mentioned above, Grt-II is characterized by higher grossular and lower spessartine contents. The X_{Fe} number shows similar values for each garnet generation. An arrow shows the inferred P–T path between the conditions of

formation of the two garnet types. Contours of modal change of garnet are not shown for clarity, but reveal that garnet will, in fact, be produced along the proposed trajectory. The absolute amount of garnet produced is impossible to quantify because of the uncertainties in the reactive rock volume.

6 MONAZITE DATING

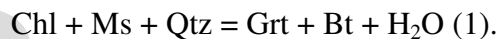
A total of 148 spot analyses performed on 69 monazite grains from the three studied samples have been used for age determination. All individual monazite data and errors (2σ) are listed in the Supporting Information Table S1.

As mentioned above, the monazites were subdivided into three compositional groups, and the weighted averages have been calculated for each group. The oldest, Mnz-I, population (high-Th) yielded an average age of 373 ± 16 Ma ($n = 13$, MSWD = 3.0; Figure 10). The second, Mnz-II, population, which is characterized by the highest Y content, yielded an age of 359 ± 6 Ma ($n = 106$, MSWD = 1.1), whereas the third, Mnz-III, population (low-Y) yielded the youngest age of 355 ± 14 Ma ($n = 29$, MSWD = 1.8).

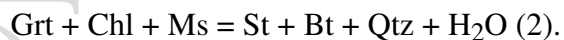
7 PETROCHRONOLOGICAL DISCUSSION

7.1 Growth of garnet-I, staurolite and kyanite

The Pinkie metapelites show a range of mineral assemblages and compositions that developed during amphibolite facies metamorphism. Petrological observations suggest that Grt-I has been produced by the following reaction (1):

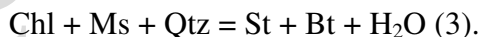


Staurolite may have formed by the reaction (2) (e.g. Spear and Cheney, 1989):

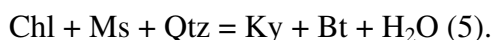
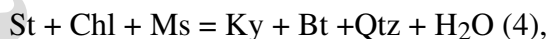


However, Grt-I shows negligible evidence for the magnitude of resorption that would be required by reaction (2). This observation suggests that garnet is only slightly reactive or even unreactive during this reaction as suggested by several authors (e.g. Hollister, 1969 a,b; Pattison & Tinkham, 2009; Pattison, De Capitani, & Gaidies, 2011; Pattison & Spear, 2018). An alternative possibility is that staurolite may have formed from a muscovite-chlorite bearing matrix via reaction (3) rather than the

garnet-consuming reaction (2) as discussed by Spear and Pattison (2017) and Pattison and Spear (2018):



In the sample KK12-5b, both kyanite and staurolite are present. Based on textural observations, there is no evidence of staurolite consumption prior to kyanite formation. Although kyanite is predicted by the petrogenetic grid to grow according to reaction (4), the lack of evidence for consumption of staurolite suggests kyanite formation from matrix minerals following reaction (5):



Moreover, there is no evidence for the former existence of staurolite in the kyanite-bearing sample KK14-33 (i.e. no inclusions or remnants in the matrix), which provides further support for the suggestion that kyanite + biotite may have formed directly from a chlorite-bearing matrix. Hence, the textural observations suggest that assemblages in the investigated metapelites were developed via the simultaneous and continuous chlorite-consuming reactions (1), (3), (5), rather than the AFM discontinuous reactions (2) and (4) as predicted by petrogenetic grids. These reactions (1, 3, and 5) would have operated until the complete consumption of chlorite.

7.2 Growth of garnet-II

The photomicrographs and X-ray maps (Figure 7) show a Grt-I porphyroblast that is surrounded by staurolite and Grt-II. Staurolite breaks down to sericite but also to garnet, which is filling the fractures in staurolite and is in contact with Grt-I. This phenomenon shows that staurolite is not a refractory phase anymore (e.g. Hollister, 1969b), thus Grt-II could have been produced according to reaction (6):

$$\text{St} + \text{Bt} + \text{Qtz} + \text{H}_2\text{O} = \text{Grt} + \text{Chl} + \text{Ms} \quad (6).$$

This hydration reaction has a positive slope on petrogenetic grids (e.g. Spear and Cheney, 1989) so it could proceed to the right with increasing pressure and decreasing temperature as inferred from the P–T path, if H₂O were present in the system.

7.3 Trace elements systematics and its implications for monazite growth

Monazite shows three chemical domains, described as high-Th Mnz-I, high-Y Mnz-II and moderate-Y Mnz-III. The oldest Mnz-I is interpreted to represent an initial early growth during advanced

diagenesis or under very low-grade metamorphic conditions early in the metamorphic cycle (e.g. Pyle, Spear, Cheney, & Layne, 2005).

High-Y Mnz-II, which is found as inclusions in garnet I and staurolite, most likely formed from the breakdown of allanite, which occurs near the staurolite and/or kyanite isograds in other terranes (e.g. Smith and Barreiro, 1990; Wing et al., 2003). This interpretation is also consistent with the Y thermometry from Mnz-II and the likelihood that xenotime was also a reactant in the monazite-producing reaction (e.g. Spear & Pyle, 2002, 2010; Yang & Pattison, 2006; Petřík & Konečný, 2009; Majka et al., 2012).

The interpretation of Mnz-III is less certain. The discontinuous Y zoning between Mnz-II and Mnz-III domains and the textural position of Mnz-III (in the matrix only) suggests that it could have been formed either during or just after the growth of the Grt-I outermost rim and may have been produced during slight resorption of Grt-I.

7.4 Formation of the fluorapatite-allanite coronas and fluid activity

The breakdown of monazite into fluorapatite-allanite coronas has been previously observed in amphibolite facies metapelites (e.g. Majka & Budzyń, 2006; Gasser, Bruand, Rubatto, & Stüwe, 2012; Lo Po et al., 2015; Figure 10). The transformation of allanite (+ apatite) to monazite was shown by Spear (2010) to have a positive slope and be a sensitive function of the bulk CaO and Al₂O₃ contents of the rock. In addition the breakdown of allanite to monazite releases H₂O so the breakdown of monazite to allanite + apatite must involve the addition of H₂O and CaO to the rock. Inasmuch as the altered monazites reflects non-coaxial strain (Fig. 9), the simplest interpretation of this texture is that it was produced during shearing along with the addition of H₂O and CaO along the P–T path from the metamorphic peak to the P–T conditions of Grt-II (Fig. 13). Dating of the breakdown corona developed around monazite would provide an estimate of the timing of the Grt-II formation, but this has not been attempted.

7.5 Pressure-temperature-time evolution

The P-T-t history of the Pinkie unit is summarized in Figure 14. Yttrium-in-monazite thermometry combined with QuiG barometry yielded P-T conditions of the Grt-I nucleation at ~ 560°C at 7.5 kbar for the staurolite-bearing sample, ~ 590°C at 9.5 kbar for the staurolite-kyanite-bearing rock, and ~ 630 °C at 10 kbar for the kyanite-bearing metapelite. The formation of Grt-II is constrained by QuiG

barometry and the trajectory indicated by the calculated garnet isopleths (Fig. 13). Based on the observation that Grt-II is not deformed, this constrains the mylonitization to have occurred at around ~ 500-550 °C and 9-11 kbar. At this stage (or before) the studied samples were likely to have been tectonically juxtaposed. . Thus, an anti-clockwise evolutionary P-T path is proposed for the Pinkie unit.

Taking into account the anticlockwise character of the deduced P-T path and the monazite dating results, it is postulated that the Pinkie unit represents a series of pelites that have undergone prograde metamorphism starting at around 373 Ma (Mnz-I) and reaching peak metamorphic conditions between *c.* 359 and 355 Ma (Mnz-II and Mnz-III) probably as the result of burial and crustal thickening, which was followed by an episode of shearing at mid crustal levels.

8 TECTONIC DISCUSSION

The present petrochronological study shows that the Pinkie unit underwent amphibolite facies metamorphism during the Ellesmerian Orogeny. The burial of the Pinkie unit could have been caused by placing a sufficient load atop the Pinkie unit, i.e. the overriding of thrust nappes in a collisional setting. Whether later shearing was associated with thrusting during ongoing collision or during late Ellesmerian shearing is impossible to reconcile based on the data presented here. It also cannot be ruled out that this mylonitisation is solely Eureka in age. However, the latter event is postulated to have not exceeded a temperature of *c.* 500°C (Schneider et al., 2019), in contrast to the results presented herein. If the mylonitization is Eureka in age, this would imply that the Bouréefjellet Fault Zone could have reactivated an already existing Ellesmerian structure. Limited access to the outcrops and challenging fieldwork conditions prevented us from collecting convincing evidence for one or the other scenario.

Nevertheless, until now the known extent of the Ellesmerian fold-and-thrust belt on Svalbard was basically restricted to the deformed Old Red Sandstone basin in northwestern and southern Spitsbergen as well as to parts of the basement areas on the west coast (Piepjohn, 2000). For the first time, the influence of the Ellesmerian Orogeny has been demonstrated on PKF. The correlation of the Pinkie unit with other amphibolite-facies metamorphic complexes occurring in western Svalbard is difficult, mostly because of limited geochronological and petrological data. The question arises as to how many portions of the basement along the west coast of Svalbard have been affected by the

Caledonian Orogeny or instead have been only or mainly affected by the Ellesmerian Orogeny. The observation that Caledonian ages on PKF are thus far missing, while Ellesmerian ages are present, indicates that the entire history of tectonic evolution in the Southwestern Basement Province of Svalbard should be re-evaluated.

Compared to the sub-greenschist or greenschist-facies metamorphism in North Greenland and parts of Ellesmere Island (e.g. Soper & Higgins, 1991; Trettin, 1991a), the rocks of the Pinkie unit have experienced the highest-grade metamorphism in the entire Ellesmerian fold-and-thrust belt documented so far. Especially in Svalbard, there is an extreme gap between the amphibolite-facies metamorphism on PKF and the brittle Ellesmerian deformation on Spitsbergen island. Some of these basement areas located along the western coast of Spitsbergen have only been affected by brittle thrusting, indicating that the Ellesmerian deformation occurred in the upper 15 km of the crust (e.g. Piepjohn 2000). The reason for this noticeable difference in crustal level across only some tens of kilometers perpendicular to strike is most probably not a feature caused by the Ellesmerian Orogeny, but an effect of the Eocene Eureka deformation and transform movement along the De Geer Line during opening of the North Atlantic and Arctic oceans (see also Piepjohn von Gosen & Tessensohn, 2015; Barnes and Schneider 2019).

The observations made on PKF have shown that at least parts of the basement units of the westernmost coast of Svalbard were involved in the Ellesmerian Orogeny. Although the driving mechanism for this orogeny and plate tectonic configurations during this event are still not satisfactorily known, structural data from Ellesmere Island, North Greenland and Svalbard indicates that the Ellesmerian Orogeny may be the result of the approach and docking of the Pearya Terrane and Svalbard on one side to the northern margin of Laurentia including the Canadian Arctic Archipelago and North Greenland (e.g. Bjørnerud & Bradley, 1994). It is possible that prior to the Ellesmerian Orogeny, in the latest Silurian and Devonian, the approach of Pearya together with Svalbard to Laurentia was the result of sinistral transform movement (Piepjohn et al., 2013), while the final orthogonal (?) docking happened during the Tournaisian. Consequently, the basement areas of western Svalbard (including the PKF), most likely were situated between the Ellesmerian fold-and-thrust belt on Svalbard on the one hand and the Laurentian margin (North Greenland and Ellesmere Island) on the other hand.

9 FINAL REMARKS AND CONCLUSIONS

An anti-clockwise P-T path is proposed for the mylonitised schists of the Pinkie unit cropping out on Prins Karls Forland (Svalbard). This includes garnet growth under amphibolite facies conditions at 7.5-10 kbar and 570-630°C followed by mylonitisation at ~ 500-550 °C and 9-11 kbar. The approach presented here, involving application of inclusion elastic barometry coupled with trace element thermometry and calculated garnet isopleths using differential thermodynamics allowed for successful estimation of P-T conditions for highly strained rocks that consist of assemblages formed during different stages of metamorphism. The P-T results together with *in-situ* Th-U-total Pb monazite dating suggests that the Pinkie unit experienced amphibolite-facies metamorphism at c. 359-355 Ma during the Ellesmerian Orogeny.

The Pinkie rocks are the first geological unit in Svalbard where Ellesmerian metamorphism has been documented and dated and the deepest geological expression the Ellesmerian Orogeny yet documented. This discovery implies that the Ellesmerian Orogeny was not limited to the brittle deformation previously described (e.g. Piepjohn et al., 2015), but it was associated with much deeper crustal processes that occurred at least up to amphibolite-facies conditions. Hence, the results presented here provide the very first evidence for the existence of an Ellesmerian crystalline basement, a hitherto missing puzzle-piece of the High Arctic continental crust.

ACKNOWLEDGMENTS

This work was supported by National Science Centre (Poland) research project Preludium no. 2013/11/N/ST10/00357, Fulbright Junior Advanced Research Award and Research Council of Norway AFG Project No. 235467/E10, RiS ID: 6571 to K. Kościńska, NSF grant 1447468 to F. S. Spear and National Science Centre (Poland) project no. 2015/17B/ST10/03114 to J. Majka. The fieldwork in 2013 and 2014 was organized by Winfried Dallmann and Synnøve Elvevold in the frame of the Geological mapping program for Svalbard (RiS ID: 2403). Henning Lorenz, the expedition leader of the reconnaissance fieldwork in 2012 in frame of the NOA-Svalbard project funded by the Swedish Polar Research Secretariat, is greatly acknowledged. Patrik Konečný and Adam Włodek are thanked for their help with electron microprobe analyses. Adrian Castro and Oliver Wolfe are warmly

Accepted Article

acknowledged for their help with Raman measurements. We thank the AirLift company for their helicopter support, which allowed us to get to the highest part of the Pinkie unit. We also thank Gregory Dumond, Deta Gasser, Evangelos Moulas and the editor Bernardo Cesare for their comments and suggestions that greatly improved the manuscript.

REFERENCES

- Angel, R.J., Mazzucchelli, M.L., Alvaro, M., Nimis, P., & Nestola, F. (2014). Geobarometry from host-inclusion systems: The role of elastic relaxation. *American Mineralogist*, 99(10), 2146-2149.
- Angel, R. J., Alvaro, M., Miletich, R., & Nestola, F. (2017a). A simple and generalised P–T–V EoS for continuous phase transitions, implemented in EosFit and applied to quartz. *Contributions to Mineralogy and Petrology*, 172(5), 0. <https://doi.org/10.1007/s00410-017-1349-x>
- Angel, R. J., Mazzucchelli, M. L., Alvaro, M., & Nestola, F. (2017b). EosFit-Pinc: A simple GUI for host-inclusion elastic thermobarometry. *American Mineralogist*, 102(9), 1957–1960. <https://doi.org/10.2138/am-2017-6190>
- Ashley, K.T., Caddick, M.J., Steele-MacInnis, M.J., Bodnar, R.J., & Dragovic, B. (2014). Geothermobarometric history of subduction recorded by quartz inclusions in garnet. *Geochemistry, Geophysics, Geosystems*, 15(2), 350-360.
- Barnes, C.J., & Schneider, D.A., 2019. Cretaceous-Paleogene low temperature history of the Southwestern Province, Svalbard, revealed by (U-Th)/He thermochronometry: implications for High Arctic tectonism. In: Piepjohn, K., Strauss, J., McClelland W. (eds), *Circum-Arctic Structural Events: Tectonic Evolution of the Arctic Margins and Trans-Arctic Links with Adjacent Orogens*: GSA Special Paper 541, doi:10.1130/2018.2541(07).
- Barnes C.J., Walczak K., Janots E., Schneider D., & Majka J. 2020. Timing of Paleozoic Exhumation and Deformation of the High-Pressure Vestgötabreen Complex at the Motalafjella Nunatak, Svalbard. *Minerals*, 10, 125, doi:10.3390/min10020125.
- Berman, R.G. (1988). Internally-Consistent Thermodynamic Data for Minerals in the System Na₂O-K₂O-CaO-MgO-FeO-Fe₂O₃-Al₂O₃-SiO₂-TiO₂-H₂O-CO₂. *Journal of Petrology*, 29(2), 445-522.
- Birkenmajer, K. (1964). Devonian, Carboniferous and Permian formations of Hornsund, Vestspitsbergen. *Studia Geologia Polonica*, 11, 47-123.
- Bjørnerud, M.G., & Bradley, D.C. (1994). Silurian foredeep and accretionary prism in northern Ellesmere Island: Implications for the nature of the Ellesmerian Orogen, in Thurston, D., & Fujita, K., ed., Proceedings of the 1992 International Conference on Arctic Margins. OCS Study MMS 94-0040, 129-133.

- Braathen, A., Osmundsen, P.T., Maher, H., & Ganerød, M. (2018). The Keisarhjelmen detachment records Silurian-Devonian extensional collapse in Northern Svalbard. *Terra Nova*, 30(1), 34-39.
- Cardozo, N., & Allmendinger, R. (2013). Spherical projections with OSXStereonet. *Computers & Geosciences*, 51, 193–205.
- Colpron, M., & Nelson, J.A.L. (2011). A Palaeozoic NW Passage and the Timanian, Caledonian and Uralian connections of some exotic terranes in the North American Cordillera. *Geological Society, London, Memoirs*, 35 (1), 463-484.
- Dallmann, W.K. (1992). Multiphase tectonic evolution of the Sørkapp-Hornsund mobile zone (Devonian, Carboniferous, Tertiary), Svalbard, in Dallmann, W. K., Andresen, A. & Krill, A., ed., Post-Caledonian Tectonic Evolution of Svalbard. *Norsk Geologisk Tidsskrift*, 72, 49-66.
- Dallmann, W.K., Birkenmajer, K., Hjelle, A., Mørk, A., Ohta, Y., Salvigsen, O., & Winsnes, T.S. (1993). Geological Map of Svalbard 1: 100,000. Sheet C13G Sørkapp (Description). *Norsk Polarinstitutt Temakart*, 17, 1-73.
- Dallmann, W.K., eds., (2015). Geoscience Atlas of Svalbard. *Norsk Polarinstitutt Rapportserie* 148, 286 p.
- Dawes, P.R. (1971). Precambrian to Tertiary of northern Greenland, in Escher, W. & Watt, W.S., ed., Geology of Greenland. *Geological Society of Greenland*, 248-303.
- Dawes, P.R., & Soper, N.J. (1973). Pre-Quaternary history of North Greenland. in Pitcher, M.G., ed., Arctic Geology. *Memoirs of the American Association of Petroleum Geologists*, 19, 117-134.
- Eide E.A. (coordinator) 2002. BATLAS. Mid Norway plate reconstruction atlas with global and Atlantic perspectives. Trondheim: Geological Survey of Norway. 75 pp.
- Enami, M., Nishtyama, T., & Mouri, T. (2007). Laser Raman microspectrometry of metamorphic quartz: A simple method for comparison of metamorphic pressures. *American Mineralogist*, 92, 1303–1315.
- Friend, P.F. (1961). The Devonian stratigraphy of north and central Vestspitsbergen. *Proc Yorkshire Geological Society*, 33, 77–118.

- Friend, P.F., Heintz, N., & Moody-Stuart, M. (1966). New unit terms for the Devonian of Spitsbergen and a new stratigraphical scheme for the Wood Bay Formation. *Norsk Polarinstitut Årbok*, 1965, 59-64.
- Gasser, D., Bruand, E., Rubatto, D., & Stüwe, K. (2012). The behaviour of monazite from greenschist facies phyllites to anatectic gneisses: an example from the Chugach Metamorphic Complex, southern Alaska. *Lithos*, 134, 108–122.
- Gee, D.G. & Moody-Stuart, M., (1966). The base of the Old Red Sandstone in central north Haakon VII Land, Vestspitsbergen. *Norsk Polarinstitut Årbok*, 1964, 57–68.
- Guiraud, M., & Powell, R., (2006). P–V–T relationships and mineral equilibria in inclusions in minerals. *Earth and Planetary Science Letters*, 244, 683–694.
- Harland, W.B., eds., (1997). The Geology Of Svalbard. *Geological Society, London, Memoirs*, 17, 514 p.
- Harland, W.B., Horsfield, W.T., Manby, G.M., & Morris, A.P. (1979). An outline of the pre-Carboniferous stratigraphy of western Central Spitsbergen. *Norsk Polarinstitut Skrifter*, 167, 119-144.
- Harrison, C., Fox, F.G., & Okulitch, A.V. (1991). Late Devonian - Early Carboniferous deformation of the Parry Islands and Canrobert Hills fold belts, Bathurst and Melville islands, in Trettin, H.P., ed., Geology of the Innuitian Orogen and Arctic Platform of Canada and Greenland. *Geological Survey of Canada, Geology of Canada*, 3, 321 - 333.
- Hjelle, A., Ohta, Y., & Winsnes, T. S. (1979). Hecla Hoek rocks of Oscar II Land and Prins Karls Forland. Svalbard. *Norsk Polarinstitut Skrifter*, 167, 145-169.
- Hjelle, A., Piepjohn, K., Saalman, K., Ohta, Y., Salvigsen, O., Thiedig, F., & Dallmann, W. (1999). Geological map of Svalbard 1:100 000, sheet A7G Kongsfjorden, Norsk Polarinstitut Temekart nr. 30, scale 1:100,000, 1 sheet, 56p. text.
- Hollister, L. S. (1969a). Contact metamorphism in the Kwoiek Area of British Columbia: An end member of the metamorphic process. *Geological Society of America Bulletin*, 80, 2465-2494.
- Hollister, L. S. (1969b). Metastable paragenetic sequence of andalusite, kyanite, and sillimanite, Kwoiek area, British Columbia. *American Journal of Science*, 267(3), 352-370.
- Holtedahl, O. (1914). On the old red sandstone series of northwestern Spitsbergen. Congress Report, XIIth Session, International Geological Congress, 707–712.

- Klaper, E.M. (1990). The mid-Paleozoic deformation in the Hazen fold belt, Ellesmere Island, Arctic Canada. *Canadian Journal of Earth Sciences*, 27, 1359-1370.
- Klaper, E.M. (1992). The Paleozoic tectonic evolution of the northern edge of North America – a structural study of northern Ellesmere Island, Canadian Arctic Archipelago. *Tectonics*, 11, 854-870.
- Klaper, E.M., & Ohta, Y. (1992). Paleozoic metamorphism across the boundary between the Clements Markham fold belt and the Pearya terrane in northern Ellesmere Island, Canadian Arctic Archipelago. *Canadian Journal of Earth Sciences*, 30(4), 867-880.
- Knoll, A.H. 1992: Vendian microfossils in metasedimentary cherts of the Scotia Group, Prins Karls Forland. *Palaeontology* 35 (4), 751-774.
- Kohn, M.J. (2014). “Thermobarometry”: calibration of spectroscopic barometers and thermometers for mineral inclusions. *Earth and Planetary Science Letters*, 388, 187–196.
- Konečný, P., Kusiak, M.A., & Dunkley, D.J. (2018). Improving U-Th-Pb electron microprobe dating using monazite age references. *Chemical Geology*, 484, 22-35.
- Kośmińska, K., Schneider, D.A., Majka, J., Lorenz, H., Gee, D.G., Manecki, M., & Barnes, C. (2015). Detrital zircon U-Pb geochronology of metasediments from southwestern Svalbard's Caledonian Province, EGU European Geosciences Union general assembly 2015, Geophysical Research Abstracts, 17, 11805.
- Kretz, R. (1983). Symbols for rock-forming minerals. *American Mineralogist*, 68, 271 -279.
- Lo Pò, D., Braga, R., Massonne, H.-J., Molli, G., Montanini, A., & Theye, T. (2016). Fluid-induced breakdown of monazite in medium-grade metasedimentary rocks of the Pontremoli basement (Northern Apennines, Italy). *Journal of Metamorphic Geology*, 34(1), 63-84.
- Ludwig, K. R. (2001). Isoplot/Ex version 2.49, Geochronological Toolkit for Microsoft Excel: Berkeley Geochronology Center Special Publication 1a.
- Majka, J., & Budzyń, B. (2006). Monazite breakdown in metapelites from Wedel Jarlsberg land, Svalbard - preliminary report. *Mineralogia*, 37(1), 61-69.
- Majka, J., Be'eri-Shlevin, Y., Gee, D.G., Ladenberger, A., Claesson, S., Konecny, P., & Klonowska, I. (2012). Multiple monazite growth in the Areskutan migmatite: Evidence for a polymetamorphic Late Ordovician to Late Silurian evolution in the Seve Nappe Complex of west-central Jamtland, Sweden. *Journal of Geosciences*, 57, 3–23. <https://doi.org/10.3190/jgeosci.112>

- Majka, J. & Kościńska, K. (2017). Magmatic and metamorphic events recorded within the Southwestern Basement Province of Svalbard. *Arktos*, 3: 5. <https://doi.org/10.1007/s41063-017-0034-7>
- Manby, G.M. (1986). Mid-Paleozoic metamorphism and polyphaser deformation of the Forland Complex, Svalbard. *Geological Magazine*, 123, 651-663.
- Mayr, U., de Freitas, T., Beauchamp, B., & Eisbacher, G. (1998). The geology of Devon Island north of 76°, Canadian Arctic Archipelago. *Geological Survey of Canada, Bulletin*, 526, 500 p.
- Mazur, S., Czerny, J., Majka, J., Manecki, M., Holm, D., Smyrak, A., & Wypych, A. (2009) A strike-slip terrane boundary in Wedel Jarlsberg Land, Svalbard, and its bearing on correlations of SW Spitsbergen with the Pearya terrane and Timanide belt. *Journal of the Geological Society of London*, 166, 529–544.
- McClelland, W.C., Malone, S.J., Gosen, W. von, Piepjohn, K., & Läufer, A. (2012). The timing of sinistral displacement of the Pearya Terrane along the Canadian Arctic Margin. *German Journal of Geosciences*, 163, 251-259.
- Montel, J.-M., Foret, S., Veschambre, M., Nicollet, Ch., & Provost, A. (1996). Electron microprobe dating of monazite. *Chemical Geology*, 131, 37–53.
- Murašov, L.G., & Mokin, J.I. 1979. Stratigraphic subdivision of the Devonian deposits of Spitsbergen. *Norsk Polarinstitut Skrifter*, 167, 249-261.
- Orvin, A.K. (1940). Outline of the geological history of Spitsbergen. *Skrifter om Svalbard og Ishavet*, 78, 1–57.
- Pattison, D.R.M., & Tinkham, D.K. (2009). Interplay between equilibrium and kinetics in prograde metamorphism of pelites: An example from the Nelson aureole, British Columbia. *Journal of Metamorphic Geology*, 27(4), 249–279.
- Pattison, D.R.M., De Capitani, C., & Gaidies, F. (2011). Petrological consequences of variations in metamorphic reaction affinity: Petrological consequences of variations in metamorphic reaction affinity. *Journal of Metamorphic Geology*, 29(9), 953–977.
- Pattison, D.R.M., & Spear, F.S. (2018). Kinetic control of staurolite–Al₂SiO₅ mineral assemblages: Implications for Barrovian and Buchan metamorphism. *Journal of Metamorphic Geology*, 00, 1–24. <https://doi.org/10.1111/jmg.12302>

- Petrík, I., & Konečný, P. (2009). Metasomatic emplacement of inherited metamorphic monazite in a biotite-garnet granite from the Nízke Tatry Mountains, Western Carpathians, Slovakia: chemical dating and evidence for disequilibrium melting. *American Mineralogist*, 94, 957–974.
- Piepjohn, K. (2000). The Svalbardian/Ellesmerian deformation of the Old Red Sandstone and the pre-Devonian basement in NW Spitsbergen (Svalbard), in Friend, P.F., and Williams, B.P.J., ed., *New perspectives on the old red sandstone, Geological Society London Special Publications*, 180, 585–601.
- Piepjohn, K., & Dallmann, W.K. (2014). Stratigraphy of the uppermost Old Red Sandstone of Svalbard (Mimerdalen Subgroup). *Polar Research*, 33(1), 1-22.
- Piepjohn, K., Greving, S., Peletz, G., Thielemann, T., Werner, S., & Thiedig, F. (1997). Kaledonische und svalbardische Entwicklung im kristallinen Basement auf der Mitrahelvøya, Albert I Land, NW-Spitzbergen. *Münstersche Forschungen zur Geologie und Paläontologie*, 82, 53-72.
- Piepjohn, K., Brinkmann, L., Grewing, A., & Kerp, H. (2000). New data on the age of the uppermost ORS and the lowermost post-ORS strata in Dickson Land (Spitsbergen) and implications for the age of the Svalbardian deformation), in Friend, P.F., and Williams, B.P.J., ed., *New perspectives on the old red sandstone, Geological Society London Special Publications*, 180, 603–609.
- Piepjohn, K., von Gosen, W., Tessensohn, F., & Saalman, K. (2008). Ellesmerian fold-and-thrust belt (northeast Ellesmere Island, Nunavut) and its Eureka overprint, in Mayr, U., ed., *Geology of northeast Ellesmere Island adjacent to Kane Basin and Nares Strait, Nunavut, Geological Survey of Canada Bulletin*, 592, 285–303.
- Piepjohn, K., von Gosen, W., Läufer, A., McClelland, W.C., & Estrada, S. (2013). Ellesmerian and Eureka fault tectonics at the northern margin of Ellesmere Island (Canadian High Arctic). *German Journal of Geosciences*, 164, 81–105.
- Piepjohn, K., von Gosen, W., Tessensohn, F., Reinhardt, L., McClelland, W.C., Dallmann, W., ... Harrison, J.C. (2015). Tectonic map of the Ellesmerian and Eureka deformation belts on Svalbard, North Greenland, and the Queen Elizabeth Islands (Canadian Arctic). *Arktos*, 1, 1-12.

- Piepjohm, K., von Gosen, W., & Tessensohn, F. (2016). The Eurekan deformation in the Arctic: an outline. *Journal of the Geological Society*, doi:10.1144/jgs2016-081.
- Pyle, J.M., Spear, F.S., Rudnick, R.L., & McDonough, W.F. (2001). Monazite–xenotime–garnet equilibrium in metapelites and a new monazite–garnet thermometer. *Journal of Petrology*, 42, 2083–2107.
- Pyle, J.M., Spear, F.S., Cheney, J.T., & Layne, G. (2005). Monazite ages in the Chesham Pond Nappe, SW New Hampshire, U. S. A.: Implications for assembly of central New England thrust sheets. *American Mineralogist*, v. 90, p. 592–606.
- Schmidt, C., & Ziemann, M. A. (2000). In-situ Raman spectroscopy of quartz: A pressure sensor for hydrothermal diamond-anvil cell experiments at elevated temperatures. *American Mineralogist*, 85(11-12), 1725–1734.
- Schneider, D.A., Faehnrich, K., Manecki, M., & Majka, J. (2019). $^{40}\text{Ar}/^{39}\text{Ar}$ Geochronologic evidence of Eurkean deformation within the West Spitsbergen Fold and Thrust Belt. In: Piepjohm, K., Strauss, J., Reinhardt, L., McClelland, W. (eds), *Circum-Arctic Structural Events: Tectonic Evolution of the Arctic Margins and Trans-Arctic Links with Adjacent Orogens*: GSA Special Paper 541, in press, 10.1130/2018.2541(08).
- Smith, H. A. & Barreiro, B., (1990). Monazite U-Pb dating of staurolite grade metamorphism in pelitic schists. *Contributions to Mineralogy and Petrology*, 105, 602-615.
- Soper, N.J., & Higgins, A.K. (1991). Late Cretaceous–Early Tertiary deformation, North Greenland. In: Trettin, H.P. (ed.) *Geology of the Innuitian Orogen and Arctic Platform of Canada and Greenland*. *Geological Survey of Canada, Geology of Canada*, 3, 461–465.
- Spear, F.S. (1988). The Gibbs method and Duhem’s theorem: The quantitative relationships among P, T, chemical potential, phase composition and reaction progress in igneous and metamorphic systems. *Contributions to Mineralogy and Petrology*, 99, 249–256.
- Spear, F.S. (1993). *Metamorphic phase equilibria and pressure-temperature-time paths*: Mineralogical Society of America. 799 pp.
- Spear, F. S., (2010). Monazite-allanite phase relations in metapelites. *Chemical Geology*, 279, 55-62.
- Spear, F.S. and Cheney, J.T. (1989). A petrogenetic grid for pelitic schists in the system SiO_2 - Al_2O_3 - FeO - MgO - K_2O - H_2O . *Contributions to Mineralogy and Petrology*, 101, 149-164.

- Spear, F.S., & Menard, T. (1989). Program GIBBS; a generalized Gibbs method algorithm. *American Mineralogist*, 74(7–8), 942–943.
- Spear, F.S., & Pyle, J.M. (2002). Apatite, monazite and xenotime in metamorphic rocks. *Reviews in Mineralogy*, 48, 293–335.
- Spear, F.S., & Pyle, J.M. (2010). Theoretical modeling of monazite growth in a low-Ca metapelite. *Chemical Geology*, 273, 111–119.
- Spear, F.S., & Pattison D.R.M. (2017). The implications of overstepping for metamorphic assemblage diagrams (MADs). *Chemical Geology*, 457, 38-46.
- Tessensohn, F., Gosen, W. von, & Piepjohn, K. (2001). Permo-Carboniferous Slivers Infolded in the Basement of Western Oscar II Land. in Tessensohn, F., ed., Intra-Continental Fold Belts - CASE 1: West Spitsbergen, Polar Issue No. 7, Geologisches Jahrbuch, B 91, 161-199.
- Thiedig, F., & Manby, G. M. (1992). Origins and deformation of post-Caledonian sediments on Blomstrandhalvøya and Lovénøyane, NW-Spitzbergen. in Dallmann, W. K., Andresen, A. & Krill, A., ed., Post-Caledonian tectonic evolution of Svalbard. *Norsk Geologisk Tidsskrift*, 72, 27-35.
- Thomas, J. B., & Spear, F. S. (2018). Experimental study of quartz inclusions in garnet at pressures up to 3.0 GPa: evaluating validity of the quartz-in-garnet inclusion elastic thermobarometer. *Contributions to Mineralogy and Petrology*, 173(5), 42. <https://doi.org/10.1007/s00410-018-1469-y>
- Thorsteinsson, R., & Tozer, E.T. (1970). Geology of the Arctic Archipelago. in Douglass, R.J.W., ed., Geology and Economic Minerals of Canada. *Geological Survey of Canada, Economic Geology Report*, 1, 547-590.
- Trettin, H.P. (1991a). Tectonic Framework, in Trettin, H.P., ed., Geology of the Innuitian Orogen and Arctic Platform of Canada and Greenland, *Geological Survey of Canada*, 3, 59-66.
- Trettin, H.P. (1991b). Late Silurian—early Devonian deformation, metamorphism, and granitic plutonism, northern Ellesmere and Axel Heiberg islands, in Trettin, H.P., ed., Geology of the Innuitian Orogen and Arctic Platform of Canada and Greenland, *Geological Survey of Canada*, 3, 295–301.

- Vogt, T. (1936). Orogenesis in the region of Paleozoic folding of Scandinavia and Spitsbergen, In: 16th International Geological Congress, Report 2, International Geological Congress, Washington, 953-955.
- Vogt, T. (1938). The stratigraphy and tectonics of the Old Red formations of Spitsbergen. *In: Abstracts of the Proceedings of the Geological Society of London*, 1343, 88.
- Yang, P., & Pattison, D. (2006). Genesis of monazite and Y zoning in garnet from the Black Hills, South Dakota. *Lithos*, 88, 233-253.
- Wing, B. A., Ferry, J. M. & Harrison, M.,(2003). Prograde destruction and formation of monazite and allanite during contact and regional metamorphism of pelites: petrology and geochronology. *Contributions to Mineralogy and Petrology*, 145, 228-250.
- Wolfe, O.M., & Spear, F.S. (2018). Determining the amount of overstepping required to nucleate garnet during Barrovian regional metamorphism, Connecticut Valley Synclinorium. *Journal of Metamorphic Geology*, 36(1), 79-94.

FIGURE CAPTIONS

Figure 1. Map showing the plate tectonic situation in the Early Eocene, at the time of magnetic anomaly 24. The extent of Caledonian and Ellesmerian fold belts as well as the Eurekan deformations are shown (Dallmann, 2015 after Batlas, 2002 and Piepjohn et al., 2013).

Figure 2. (a) Overview map of the Svalbard Archipelago with location of the studied area marked by pink rectangle (Gee & Tebenkov, 2004, modified). The localities discussed in the text are marked on the map: KF – Kongsfjorden, OIIL – Oscar II Land, PKF – Prins Karls Forland, SJF – St. Jonsfjorden; (b) Geological map of the Grimaldibukta area. Sample locations are indicated by stars (Dallmann, 2015, modified); (c) Equal area projections of structural elements in the study area, shown are lineation measurements and poles to foliation with Kamp contours indicating density of measured directions. Plots made in Stereonet 10.0 (Cardozo & Allmendiger, 2013).

Figure 3. (a) NW-slopes of the Bouréefjellet mountain, the locations of studied samples are marked by stars; (b) The Pinkie unit mylonitised metapelites, sample KK14-35, 1 Norwegian krone for scale.

Figure 4. Photomicrographs of the Pinkie unit metapelites. (a) Staurolite overgrowing garnet-I, sample KK14-35; (b) Staurolite overgrowing garnet-I, sample KK14-35; (c) Staurolite-kyanite-garnet-bearing metapelite KK12-5b; (d) Staurolite porphyroblast and kyanite aggregate surrounded by foliation composed of muscovite, biotite and quartz, sample KK12-5b; (e) Kyanite fine grained aggregates within the foliation plane, sample KK14-33; (f) Partially replaced garnet porphyroblasts, kyanite, biotite, muscovite and quartz in the matrix, sample KK14-33; (g) Kyanite breaking down to sericite, sample YO72 598; (h) Subhedral to euhedral crystals of garnet-II, sample KK14-35.

Figure 5. Compositional maps of garnet from sample KK14-35, KK12-5b and KK14-33. Major element X-ray maps of Fe, Mg, Ca, Mg. Simplified sketch showing the Grt-I and Grt-II is shown as well.

Figure 6. (a) – (d) Back-scattered electron (BSE) images of garnet porphyroblasts. An arrow indicates a WDS stepscan profile through garnet. (e) – (h) Compositional profile through garnet crystals, variations in almandine (Alm), spessartine (Sps), pyrope (Prp), grossular (Grs) and iron number (X_{Fe}) are shown. Dotted lines and grey shades are indicating the difference between the composition of garnet-I (Grt-I) and garnet-II (Grt-II). Lower part of the diagram is a close up of Grs and Sps trends to better show the compositional difference. $X_{Fe} = Fe/(Fe+Mg)$

Figure 7. (a, b) Photomicrographs of the Grt-I-St-Grt-II texture from sample KK14-35; (a-b) Garnet-I (Grt-I) is overgrown by staurolite (St), which is breaking down to sericite (Se). Garnet-II (Grt-II) overgrows staurolite and fills cracks, (c-f) X-ray chemical maps for calcium, manganese, iron magnesium ratio (X_{Fe}) and aluminum.

Figure 8. Back-scattered electron (BSE) images, Th, Y chemical maps and simplified sketches of representative monazite grains. Warmer colors indicate higher concentration of elements.

Figure 9. Backscattered electron images showing monazite (Mnz) breaking down to allanite (Aln) and apatite (Ap): (a) sample KK14-35, (b) sample KK12-5b.

Figure 10. (a) Binary Th vs. Y (wt. %) diagram for monazite from studied metapelites. Three chemical populations and weighted-mean age are shown; (b) Back-scattered electron (BSE) image is showing the textural position of each population; (c) weighted mean plot for individual monazite analyses.

Figure 11. Quartz-in-garnet (QuiG) Raman results: (a) Positions for the 464 cm^{-1} Raman peak for quartz inclusions in garnet from Pinkie unit samples; (b) P-T diagram showing the results of QuiG barometry and Y-in-monazite thermometry.

Figure 12. Yttrium X-ray map of garnet overgrown by staurolite, sample KK14-35.

Figure 13. Calculated phase equilibria for the Pinkie unit metapelite sample KK14-35. Compositional isopleths are shown for Grt-I (solid lines) and Grt-II (dashed lines). Contours are drawn relative to the reference P–T conditions indicated by the star. The black arrow is the inferred P–T path constrained by the compositions of Grt-I and Grt-II.

Figure 14. Pressure-temperature-time (P-T-t) evolutionary path for Pinkie unit metapelites. Quartz-in-garnet (QuiG) barometry, trace-element thermometry and the results of calculated phase equilibria are shown. The growth of monazite during prograde metamorphism is indicated by ellipse. The breaking down of the monazite is shown by simplified sketch on the retrograde path.

TABLE CAPTIONS

Table 1 – GPS coordinates of the studied sample

Table 2 – Representative analyses of garnet.

Table 3 – Representative analyses of staurolite, muscovite, biotite and plagioclase

Table 4 – Representative analyses of monazite.

SUPPORTING DATASET

Table S1 – Measured Th, U, Pb concentrations, Th* values, ages and 1 sigma errors for dated monazite samples.

Table 1 – GPS coordinates of the studied sample

Sample ID	Mineral assemblage	GPS coordinates
KK14-35	Grt+Ms+Bt+St+Pl+Qtz	78°43'06.2"N 10°59'02.8"E
KK12-5b	Grt+Ms+Bt+St+Ky+Pl+Qtz	78°43'04.9"N 10°58'36.9"E
KK14-33	Grt+Ms+Bt+Ky+Pl+Qtz	78°43'05.8"N 10°58'45.2"E

Table 2 – Representative analyses of garnet.

Sample ID	KK14-35	KK14-35	KK12-5b	KK12-5b	KK14-33	KK14-33	KK14-35	KK14-35	KK14-33
Mineral	Garnet-I						Garnet-II		
Text.type	rim	core	rim	core	rim	core	small grt	rim on Grt-I	rim on Grt-I
Analysis	5	88	15	53	192	92	29	195	4
SiO ₂	36.86	37.12	36.62	35.69	36.21	36.99	37.34	37.04	37.35
TiO ₂	0.00	0.08	0.03	0.00	0.04	0.03	0.06	0.03	0.04
Al ₂ O ₃	20.77	20.83	20.87	20.10	20.94	20.83	21.16	20.87	21.31
Cr ₂ O ₃	0.02	0.03	0.00	0.03	0.03	0.03	0.04	0.03	0.01
FeO	37.44	36.18	39.35	39.36	36.00	34.27	35.77	35.76	34.32
MnO	0.93	1.00	0.42	1.06	2.20	3.40	0.26	0.30	0.31
MgO	2.47	2.74	2.13	2.13	2.09	2.65	2.64	2.13	2.64
CaO	1.31	1.99	0.52	0.56	1.38	1.32	2.90	3.97	3.85
Na ₂ O	0.02	0.00	0.01	0.03	0.08	0.00	0.00	0.02	0.04
K ₂ O	0.00	0.00	0.00	0.00	0.00	0.01	0.00	0.00	0.03
Total	99.81	99.97	99.94	98.95	98.97	99.53	100.17	100.15	99.91
O	12.00	12.00	12.00	12.00	12.00	12.00	12.00	12.00	12.00
Si	2.995	2.999	2.976	2.963	2.972	3.004	2.999	2.990	2.997
Ti	0.000	0.005	0.002	0.000	0.002	0.002	0.004	0.002	0.002
Al	1.990	1.983	2.000	1.967	2.026	1.994	2.004	1.986	2.016
Cr	0.001	0.002	0.000	0.002	0.002	0.000	0.003	0.002	0.001
Fe	2.545	2.444	2.754	2.732	2.471	2.327	2.402	2.414	2.303
Mn	0.064	0.068	0.029	0.075	0.153	0.234	0.017	0.020	0.021
Mg	0.299	0.329	0.257	0.263	0.256	0.321	0.316	0.256	0.316
Ca	0.114	0.173	0.045	0.049	0.121	0.115	0.250	0.344	0.331
Na	0.002	0.000	0.002	0.005	0.014	0.000	0.000	0.003	0.007
K	0.000	0.000	0.000	0.000	0.000	0.001	0.000	0.000	0.004
Cation Total	8.010	8.003	8.065	8.056	8.017	7.997	7.994	8.016	7.997
X _{Alm}	0.842	0.811	0.889	0.876	0.824	0.777	0.805	0.796	0.775
X _{Sps}	0.021	0.023	0.010	0.024	0.051	0.078	0.006	0.007	0.007
X _{Prp}	0.099	0.109	0.086	0.084	0.085	0.107	0.106	0.084	0.106
X _{Grs}	0.038	0.057	0.015	0.016	0.040	0.038	0.084	0.113	0.111
X _{Fe}	0.895	0.881	0.915	0.912	0.906	0.879	0.884	0.904	0.880

X_{Alm} = Fe/(Fe+Mg+Ca+Mn); X_{Sps} = Mn/(Fe+Mg+Ca+Mn); X_{Prp} = Mg/(Fe+Mg+Ca+Mn); X_{Grs} = Ca/(Fe+Mg+Ca+Mn); X_{Fe} = Fe/(Fe+Mg).

Table 3 – Representative analyses of staurolite, muscovite, biotite and plagioclase.

Sample ID	KK14-35	KK12-5b	KK14-35	KK12-5b	KK14-33	KK14-35	KK12-5b	KK14-33	KK14-35	KK12-5b	KK14-33
Mineral	Staurolite		Biotite			Muscovite			Plagioclase		
Analysis	1	3	10	8	6	1	6	5	7	3	5
SiO ₂	27.23	26.83	36.91	35.00	36.85	46.51	45.36	47.17	64.65	64.24	63.46
TiO ₂	0.35	0.47	0.72	1.39	2.46	0.54	0.66	0.76	0.01	0.00	0.00
Al ₂ O ₃	53.38	53.27	18.51	18.84	19.93	35.30	35.76	34.49	21.07	21.50	23.31
Cr ₂ O ₃	0.04	0.08	0.00	0.00	0.00	0.00	0.11	0.04	0.00	0.00	0.00
FeO	13.16	13.26	19.78	20.13	19.31	0.65	0.95	1.23	0.06	0.02	0.11
MnO	0.11	0.05	0.00	0.00	0.05	0.00	0.02	0.04	0.00	0.01	0.00
MgO	1.52	1.39	10.74	8.97	8.85	0.49	0.48	0.56	0.00	0.00	0.00
CaO	0.00	0.00	0.01	0.04	0.07	0.01	0.01	0.01	2.09	2.33	4.95
Na ₂ O	0.00	0.05	0.10	0.15	0.06	1.44	1.63	1.19	10.68	10.58	8.79
K ₂ O	0.05	0.00	8.86	8.31	8.95	8.52	8.64	9.34	0.08	0.06	0.07
BaO	n.d.	n.d.	n.d.	0.00	0.00	n.d.	0.16	0.29	n.d.	0.00	0.00
ZnO	0.20	0.56	n.d.	n.d.	n.d.	n.d.	n.d.	n.d.	n.d.	n.d.	n.d.
Total	96.03	95.94	95.62	92.83	96.53	93.44	93.79	95.12	98.64	98.74	100.69
O	23.00	23.00	11.00	11.00	11.00	11.00	11.00	11.00	8.00	8.00	8.00
Si	3.844	3.803	2.782	2.729	2.738	3.108	3.037	3.134	2.885	2.866	2.784
Ti	0.037	0.050	0.041	0.082	0.120	0.892	0.033	0.038	0.000	0.000	0.000
Al	8.881	8.897	1.645	1.732	1.789	1.915	2.822	2.700	1.109	1.131	1.209
Cr	0.004	0.009	0.000	0.000	0.000	0.000	0.006	0.002	0.000	0.000	0.000
Fe	1.553	1.571	1.247	1.312	1.157	0.036	0.053	0.068	0.002	0.001	0.000
Mn	0.014	0.006	0.000	0.000	0.000	0.000	0.001	0.002	0.000	0.000	0.000
Mg	0.319	0.293	1.206	1.042	0.981	0.049	0.048	0.056	0.000	0.000	0.000
Ca	0.000	0.000	0.001	0.003	0.002	0.000	0.001	0.000	0.100	0.111	0.238
Na	0.000	0.013	0.014	0.023	0.041	0.187	0.211	0.154	0.924	0.915	0.751
K	0.009	0.000	0.852	0.827	0.881	0.727	0.738	0.792	0.004	0.003	0.006
Ba	n.d.	n.d.	n.d.	n.d.	0.000	n.d.	0.004	0.008	n.d.	0.000	0.000
Zn	0.020	0.058	n.d.	n.d.	n.d.	n.d.	n.d.	n.d.	n.d.	n.d.	n.d.
Cation Total	14.681	14.701	7.788	7.749	7.709	6.913	6.954	6.953	5.024	5.028	4.989
X _{Ab}									0.898	0.889	0.755
X _{An}									0.097	0.108	0.239
X _{Or}									0.004	0.003	0.006
X _{Fe}	0.829	0.843	0.508	0.557	0.541						

X_{Fe} = Fe/(Fe+Mg); X_{Ab} = Na/(Na+Ca+K); X_{An} = Ca/(Na+Ca+K); X_{Or} = K/(Na+Ca+K).

Table 4 – Representative analyses of monazite.

Sample ID	KK14-35	KK12-5b	KK14-33	KK14-35	KK12-5b	KK14-33	KK14-35	KK12-5b	KK14-33
Mnz population	I	I	I	II	II	II	III	III	III
Analysis	14/1	16/2	5/1	30/2	50/1	60/3	23/1	20/2	60/2
P ₂ O ₅	29.42	29.58	28.47	29.72	30.80	29.32	29.42	29.14	29.14
SiO ₂	0.31	0.22	0.63	0.20	0.24	0.22	0.24	0.26	0.25
CaO	1.73	1.83	1.90	1.04	0.85	1.14	0.79	1.07	1.14
PbO	0.13	0.15	0.21	0.07	0.08	0.11	0.08	0.08	0.10
ThO ₂	7.12	7.71	10.32	4.28	3.67	4.67	3.52	4.78	4.98
UO ₂	0.44	0.78	0.62	0.44	0.29	0.64	0.59	0.50	0.75
Y ₂ O ₃	1.05	1.11	0.56	1.57	1.91	2.32	1.14	0.81	0.96
La ₂ O ₃	13.60	12.90	11.52	14.21	14.63	12.71	15.01	14.15	13.30
Ce ₂ O ₃	28.16	25.97	24.93	28.75	28.60	27.73	28.99	28.59	28.14
Pr ₂ O ₃	3.18	2.97	2.88	3.25	3.24	3.20	3.26	3.23	3.39
Nd ₂ O ₃	11.02	11.30	10.77	11.88	12.29	12.13	12.08	11.91	12.50
Sm ₂ O ₃	1.68	2.10	1.86	1.98	1.92	2.21	2.02	1.99	2.25
Gd ₂ O ₃	1.06	1.53	0.81	1.28	1.42	2.01	1.33	1.25	1.91
Dy ₂ O ₃	0.45	0.55	0.24	0.57	0.65	0.83	0.53	0.27	0.58
Ho ₂ O ₃	n.d.	0.01	0.02	n.d.	0.07	0.10	0.07	0.03	n.d.
Er ₂ O ₃	0.36	0.35	0.32	0.40	0.39	0.41	0.35	0.31	0.31
Yb ₂ O ₃	0.10	0.12	0.16	0.16	0.10	0.07	0.10	0.12	0.10
Total	99.81	99.17	96.21	99.79	101.14	99.80	99.51	98.51	99.82
P	5.869	5.921	5.880	5.910	5.972	5.854	5.898	5.880	5.853
Si	0.073	0.029	0.153	0.048	0.054	0.051	0.057	0.063	0.060
Ca	0.438	0.465	0.498	0.261	0.208	0.287	0.199	0.274	0.290
Pb	0.008	0.010	0.013	0.004	0.005	0.007	0.005	0.005	0.006
Th	0.382	0.415	0.573	0.229	0.191	0.251	0.190	0.259	0.269
U	0.023	0.041	0.034	0.023	0.015	0.033	0.031	0.027	0.040
Y	0.132	0.140	0.073	0.196	0.233	0.291	0.144	0.102	0.121
La	1.182	1.125	1.037	1.231	1.235	1.106	1.311	1.244	1.164
Ce	2.430	2.248	2.227	2.473	2.398	2.395	2.514	2.495	2.444
Pr	0.273	0.256	0.256	0.278	0.271	0.275	0.281	0.281	0.293
Nd	0.928	0.954	0.939	0.997	1.005	1.021	1.022	1.014	1.059
Sm	0.137	0.171	0.157	0.161	0.152	0.180	0.165	0.164	0.184
Gd	0.083	0.120	0.065	0.100	0.108	0.157	0.104	0.099	0.151
Dy	0.034	0.042	0.019	0.043	0.048	0.063	0.040	0.021	0.045
Ho	n.d.	0.001	0.002	n.d.	0.005	0.007	0.005	0.002	n.d.
Er	0.027	0.026	0.024	0.030	0.028	0.030	0.026	0.023	0.023
Yb	0.007	0.009	0.012	0.011	0.007	0.005	0.007	0.009	0.007
Cation Total	12.032	11.977	11.967	11.999	11.942	12.024	12.007	11.971	12.016
X _{LREE}	0.814	0.789	0.779	0.851	0.857	0.815	0.876	0.863	0.844
X _{HREE}	0.025	0.033	0.021	0.030	0.033	0.043	0.030	0.026	0.037
X _{hut}	-0.004	0.000	0.021	-0.001	0.000	0.001	0.004	0.003	0.004
X _{brb}	0.144	0.154	0.168	0.086	0.070	0.094	0.066	0.091	0.095
X _{YPO4}	0.022	0.023	0.012	0.032	0.039	0.048	0.024	0.017	0.020

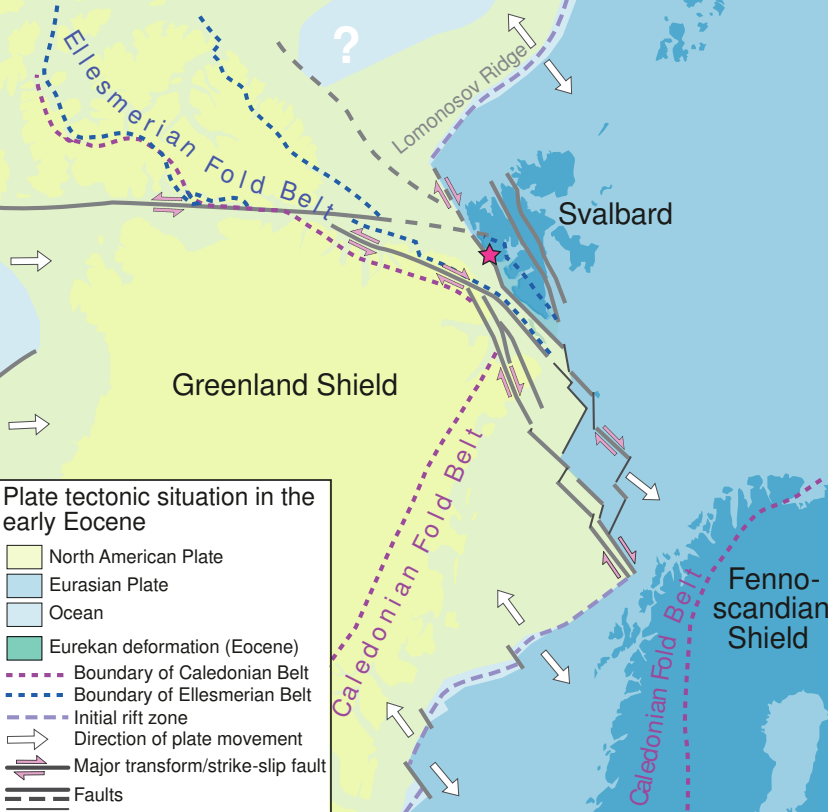
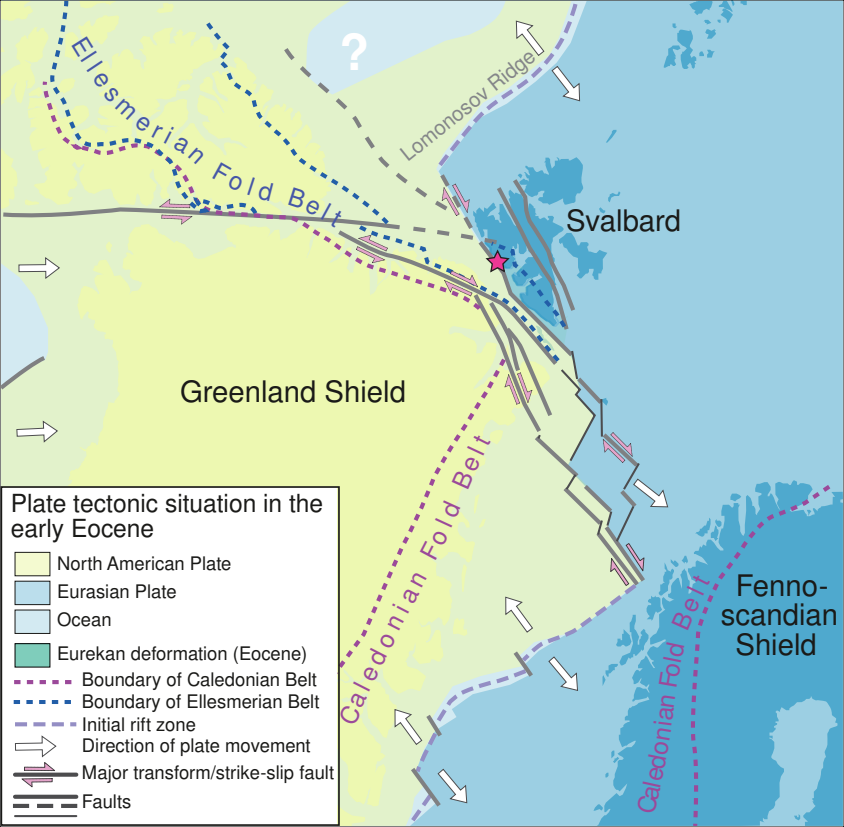


Plate tectonic situation in the early Eocene

- North American Plate
- Eurasian Plate
- Ocean
- Eureka deformation (Eocene)
- Boundary of Caledonian Belt
- Boundary of Ellesmerian Belt
- Initial rift zone
- Direction of plate movement
- Major transform/strike-slip fault
- Faults

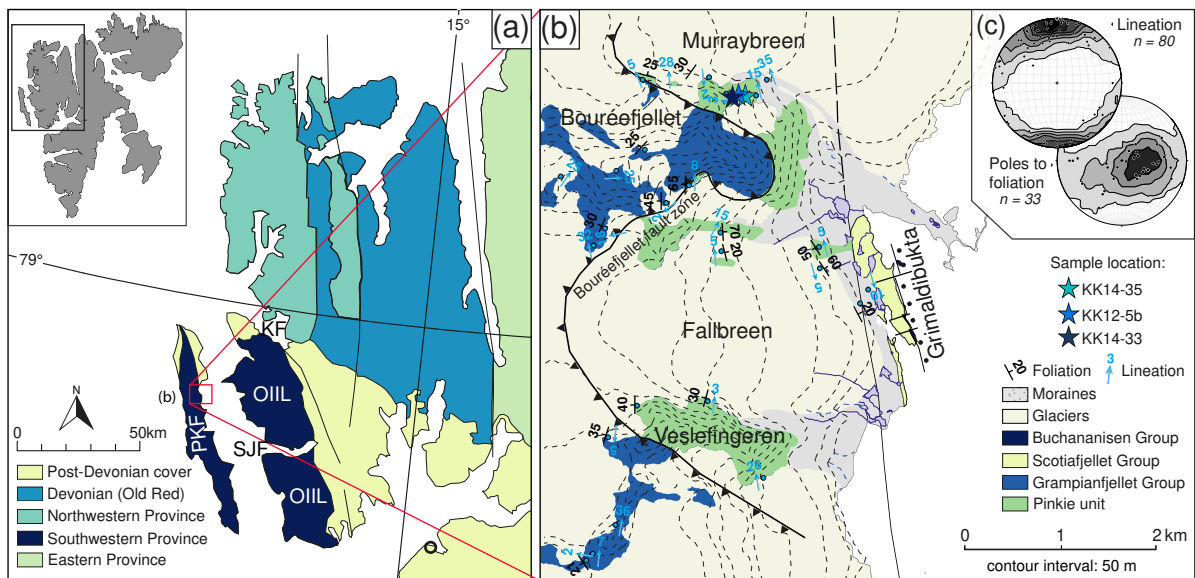


Figure 2. (a) Overview map of the Svalbard Archipelago with location of the studied area marked by pink rectangle (Gee & Tebenkov, 2004, modified). The localities discussed in the text are marked on the map: KF – Kongsfjorden, OIIL – Oscar II Land, PKF – Prins Karls Forland, SJF – St. Jonsfjorden. (b) Geological map of the Grimaldibukta area. Sample locations are indicated by stars (Dallmann, 2015, modified). (c) Equal area projections of structural elements in the study area, shown are lineation measurements and poles to foliation with Kamp contours indicating density of measured directions, plots made in Stereonet 10.0 (Cardozo & Allmendinger, 2013).

(a)



(b)

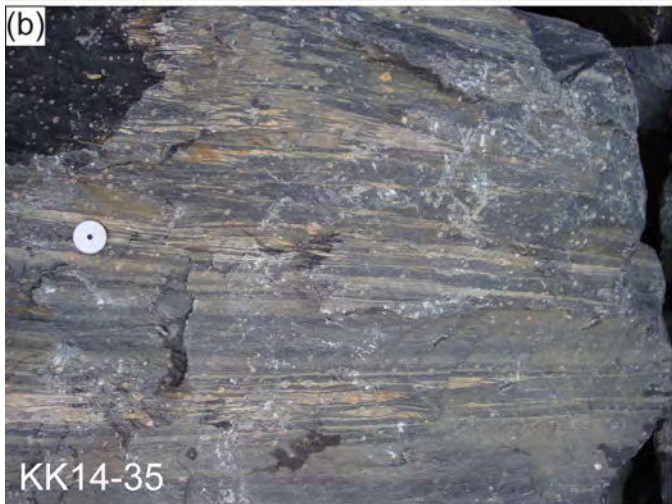


Figure 3. (a) NW-slopes of the Bouréefjellet mountain, the locations of studied samples are marked by stars; (b) The Pinkie unit mylonitised metapelites, sample KK14-35, 1 Norwegian krone for scale.

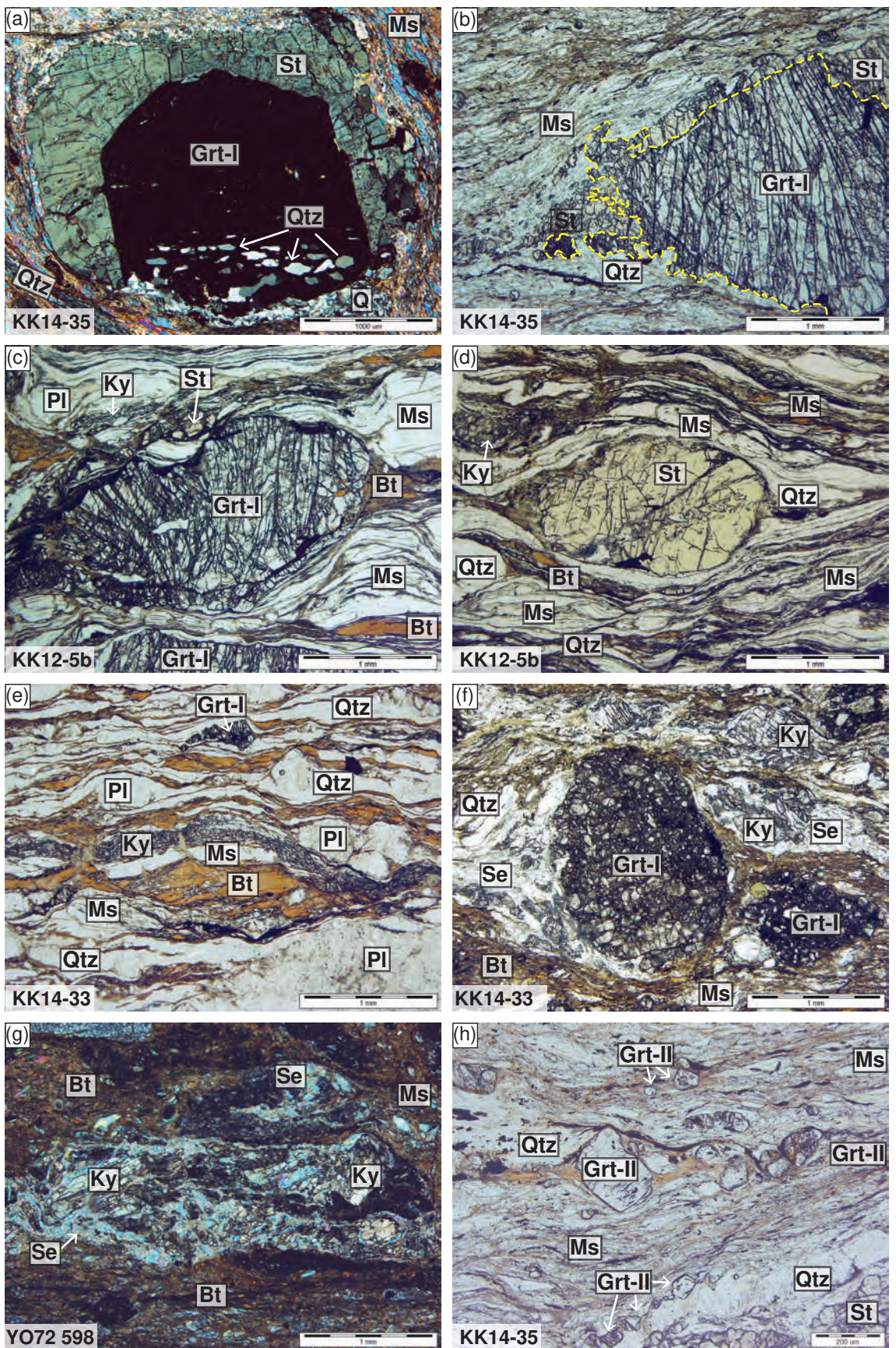


Figure 4. Photomicrographs of the Pinkie unit metapelites. (a) Staurolite overgrowing garnet-I, sample KK14-35; (b) Staurolite overgrowing garnet-I, sample KK14-35; (c) Staurolite-kyanite-garnet-bearing metapelite KK12-5b; (d) Staurolite porphyroblast and kyanite aggregate surrounded by foliation composed of muscovite, biotite and quartz, sample KK12-5b; (e) Kyanite fine grained aggregates within the foliation plane, sample KK14-33; (f) Partially replaced garnet porphyroblasts, kyanite, biotite, muscovite and quartz in the matrix, sample KK14-33; (g) Kyanite breaking down to sericite, sample YO72 598; (h) Subhedral to euhedral crystals of garnet-II, sample KK14-35.

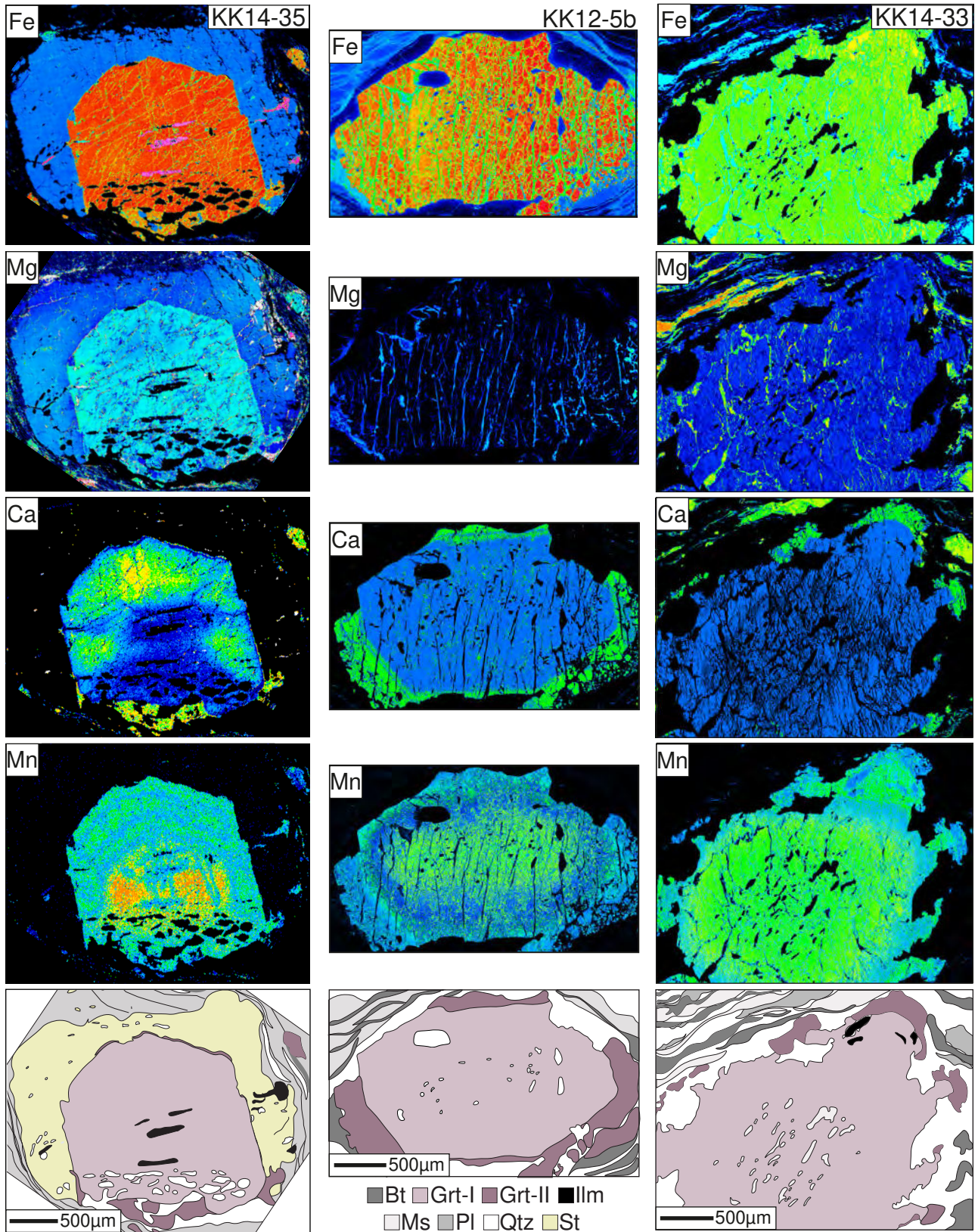


Figure 5. Compositional maps of garnet from sample KK14-35, KK12-5b and KK14-33. Major element X-ray maps of Fe, Mg, Ca, Mg. Simplified sketch showing the Grt-I and Grt-II is shown as well.

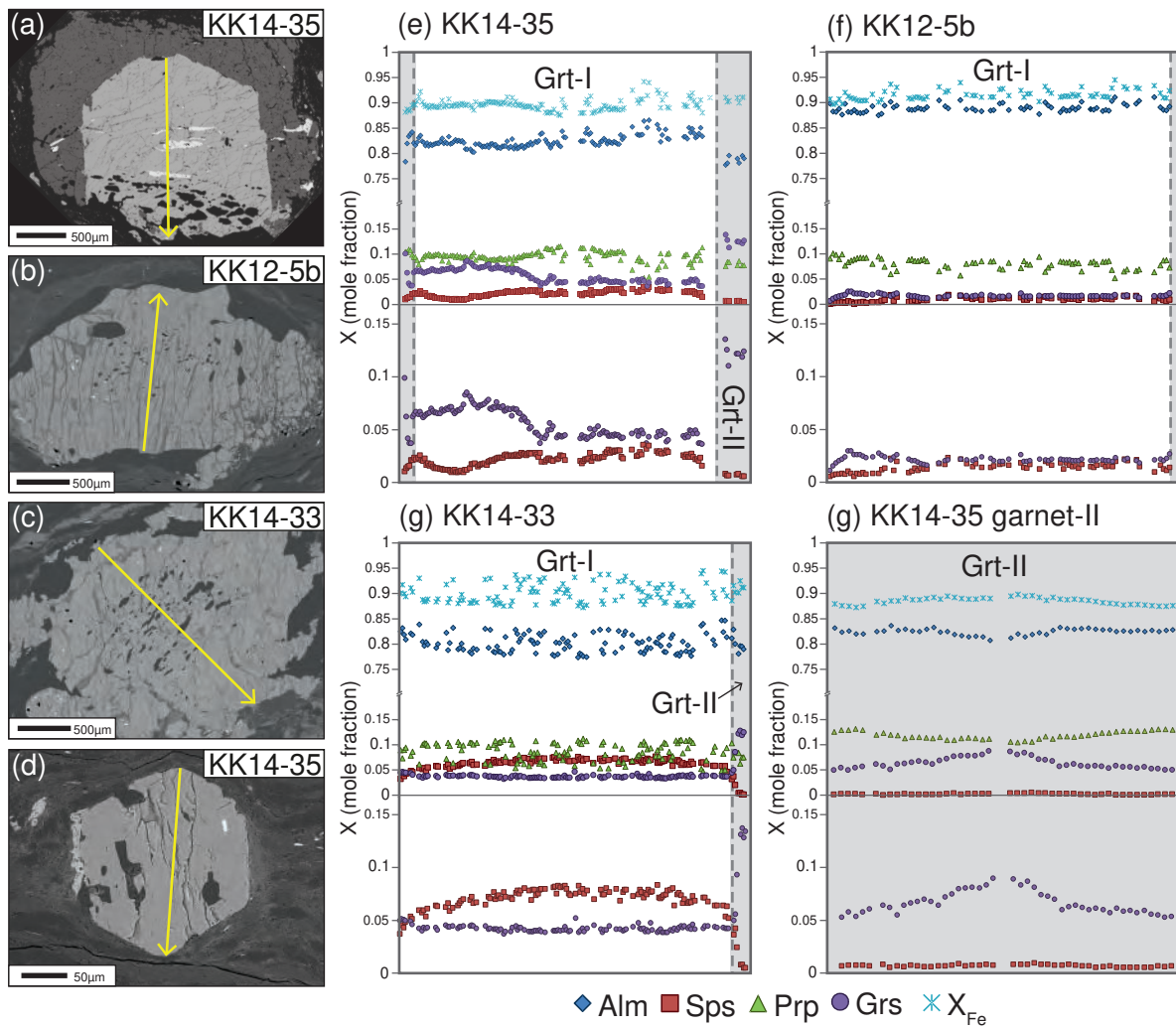


Figure 6. (a) - (d) BSE images of garnet porphyroblasts. An arrow indicates a WDS stepscan profile through garnet. (e) - (h) Compositional profile through garnet crystals, variations in almandine (Alm), spessartine (Sps), pyrope (Prp), grossular (Grs) and iron number (X_{Fe}) are shown for samples KK14-35, KK12-5b and KK14-33. Dotted lines and grey shades are indicating the difference between the composition of garnet-I (Grt-I) and garnet-II (Grt-II). Lower part of the graph is a close up of Grs and Sps trends to better show the compositional difference. $X_{Fe} = Fe/(Fe+Mg)$

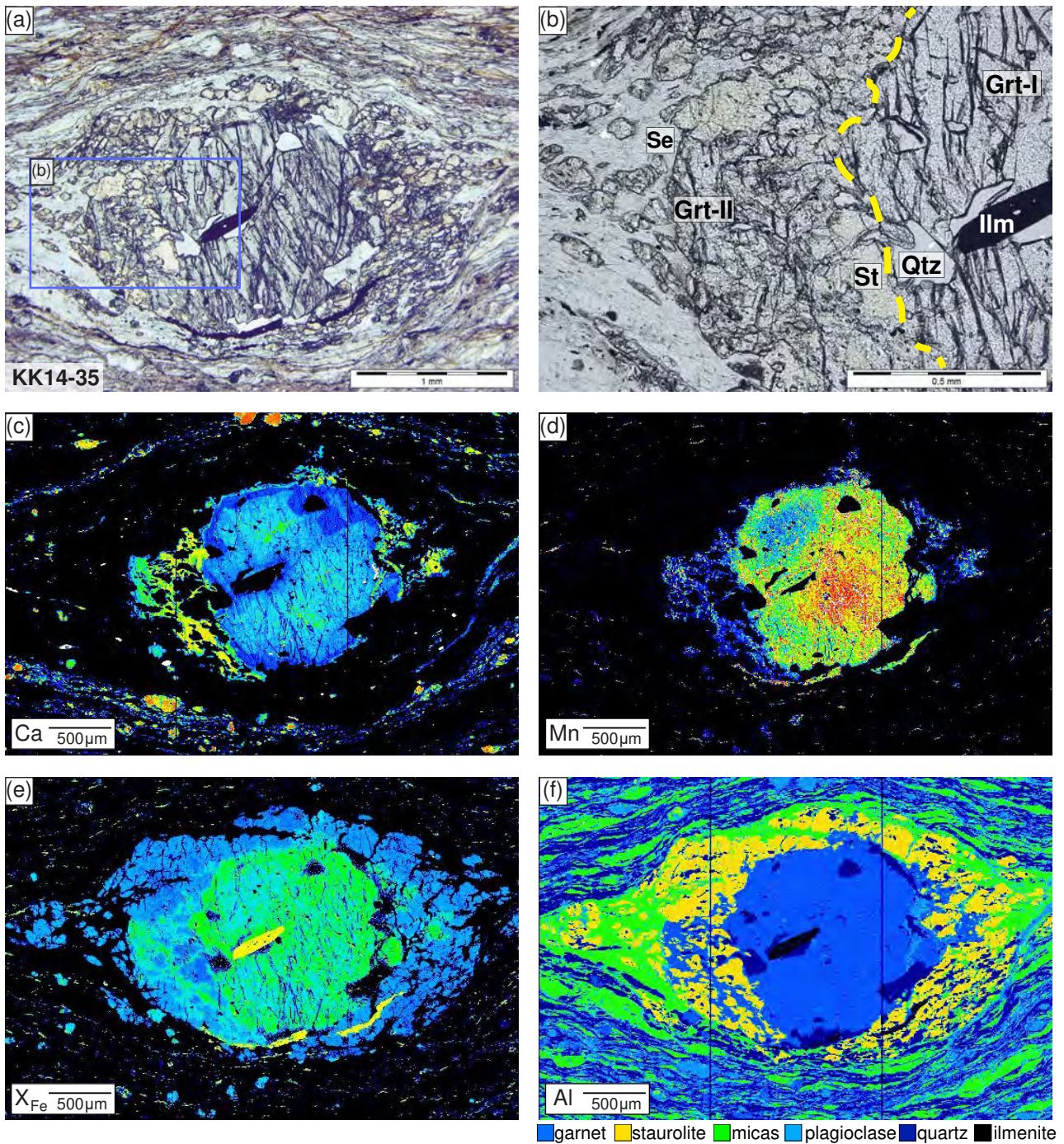


Figure 7. (a, b) Photomicrographs of the Grt-I-St-Grt-II texture from sample KK14-35; (a-b) Garnet-I (Grt-I) is overgrown by staurolite (St), which is breaking down to sericite (Se). Garnet-II (Grt-II) overgrows staurolite and fills cracks, (c-f) X-ray maps for calcium, manganese, iron magnesium ratio and aluminum.

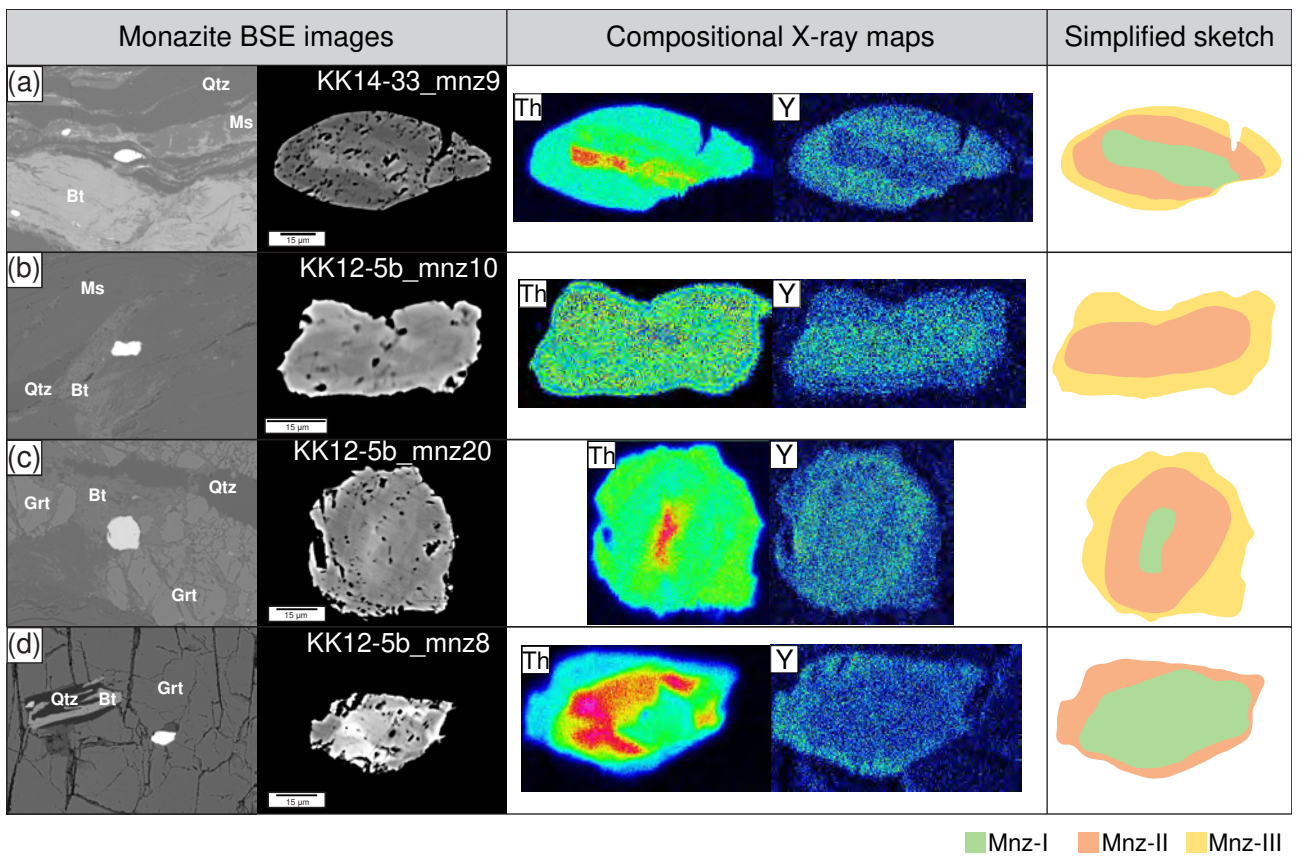


Figure 8. Back-scattered electron (BSE) images, Th, Y maps and simplified sketches of representative monazite grains. Warmer colors indicate higher concentration of elements.

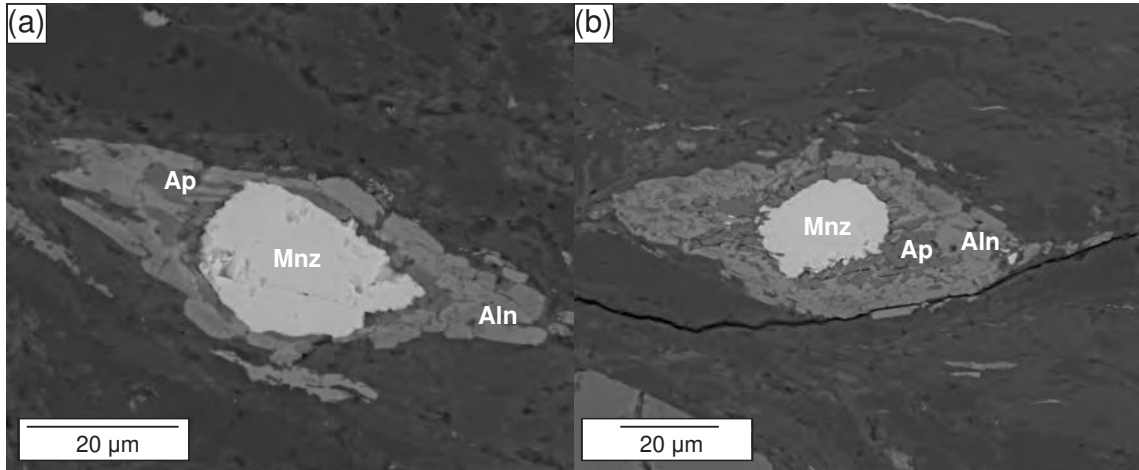


Figure 9. Backscattered electron images showing monazite (Mnz) breaking down to allanite (Aln) and apatite (Ap): (a) sample KK14-35, (b) sample KK12-5b.

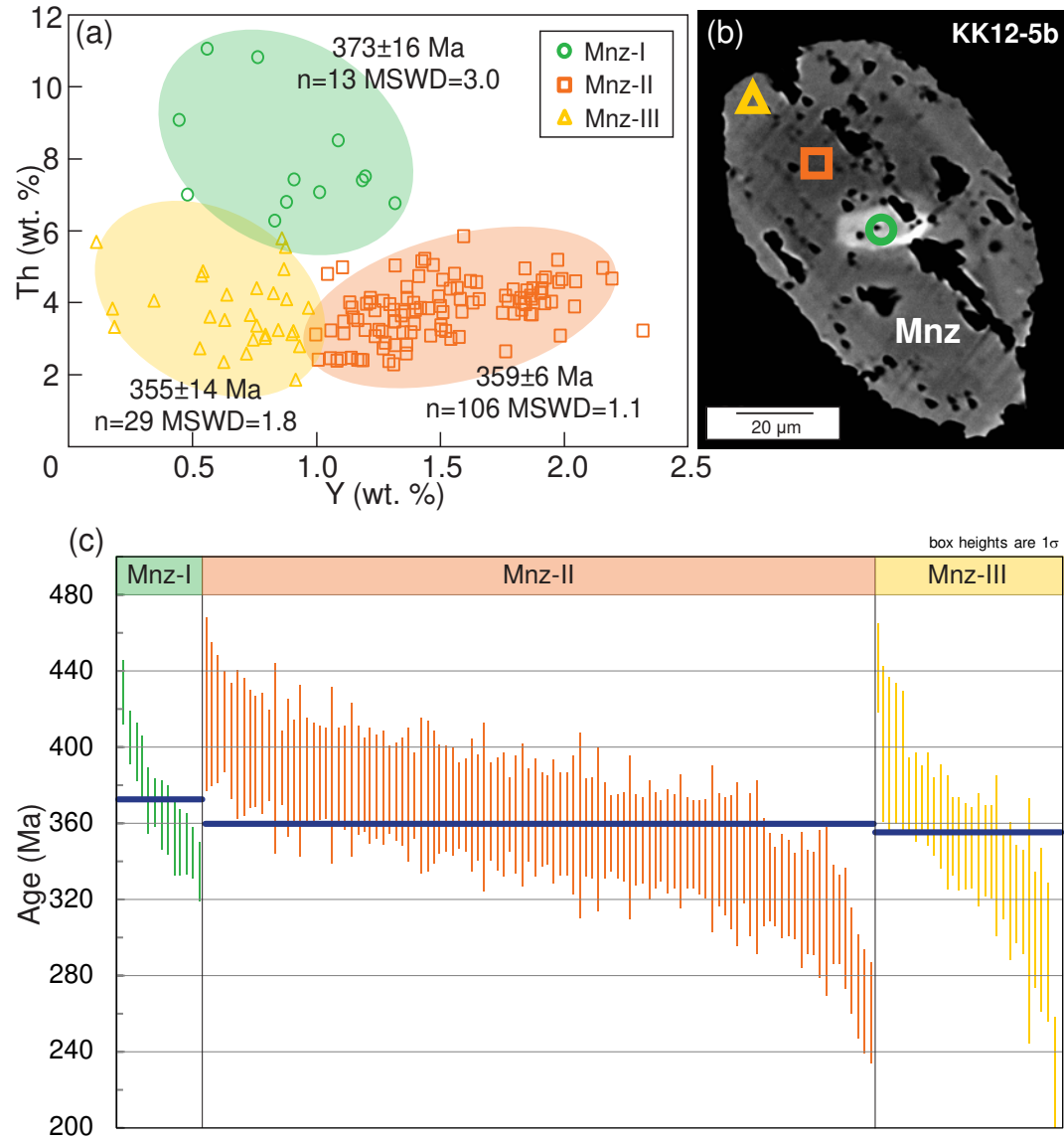


Figure 10. (a) Binary Th vs. Y (wt. %) diagram for monazite from studied metapelites. Three chemical populations and weighted-mean age are shown; (b) Back-scattered electron (BSE) image is showing the textural position of each population; (c) weighted mean age plot for individual monazite analyses.

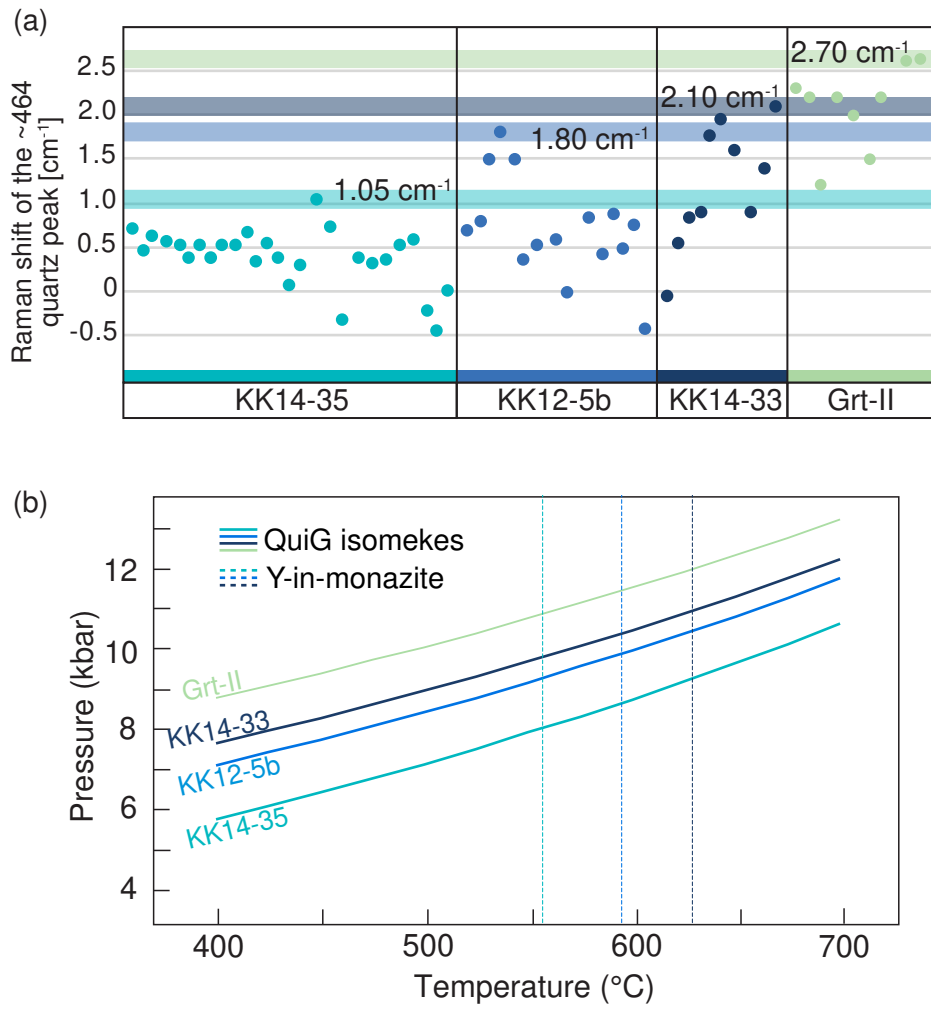


Figure 11. Quartz-in-garnet (QuiG) Raman results: (a) Positions for the 464 cm^{-1} Raman peak for quartz inclusions in garnet from Pinkie unit samples; (b) P-T diagram showing the results of QuiG barometry and Y-in-monazite thermometry.

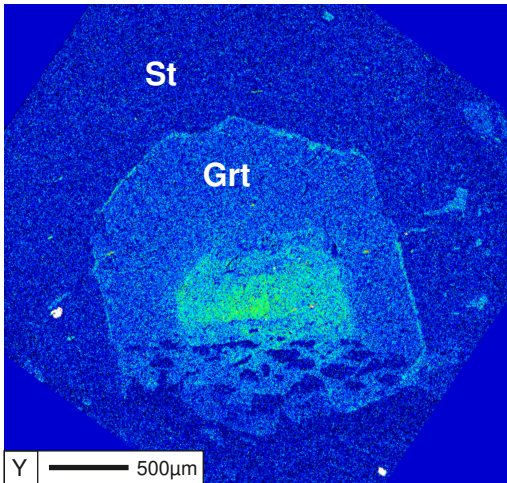


Figure 12. Yttrium X-ray map of garnet overgrown by staurolite, sample KK14-35.

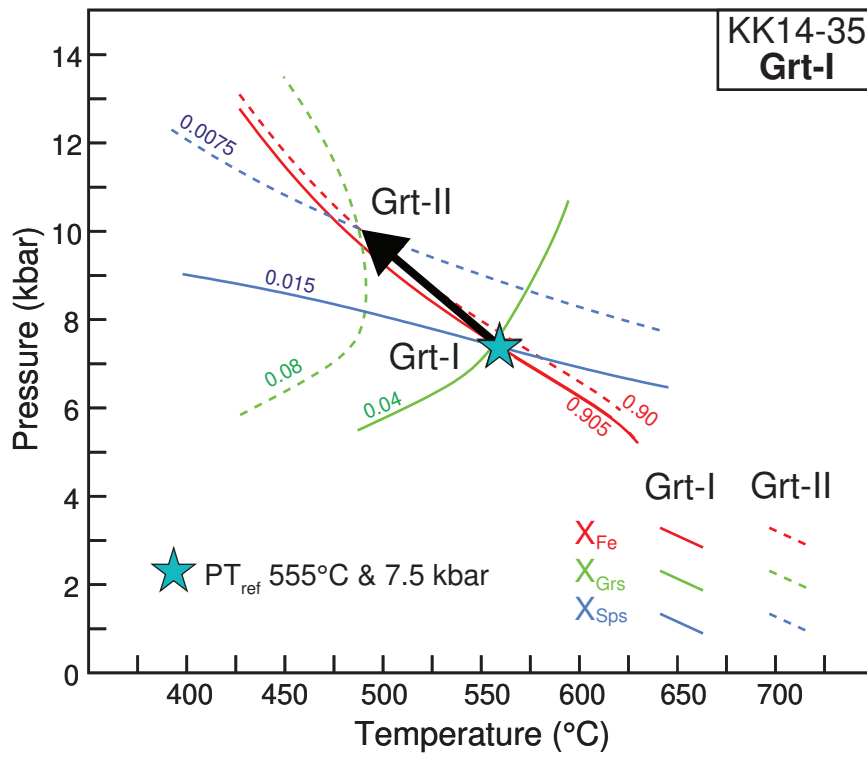


Figure 13. Calculated phase equilibria for the Pinkie unit metapelite sample KK14-35. Compositional isopleths are shown for Grt-I (solid lines) and Grt-II (dashed lines). Contours are drawn relative to the reference P–T conditions indicated by the star. The black arrow is the inferred P–T path constrained by the compositions of Grt-I and Grt-II.

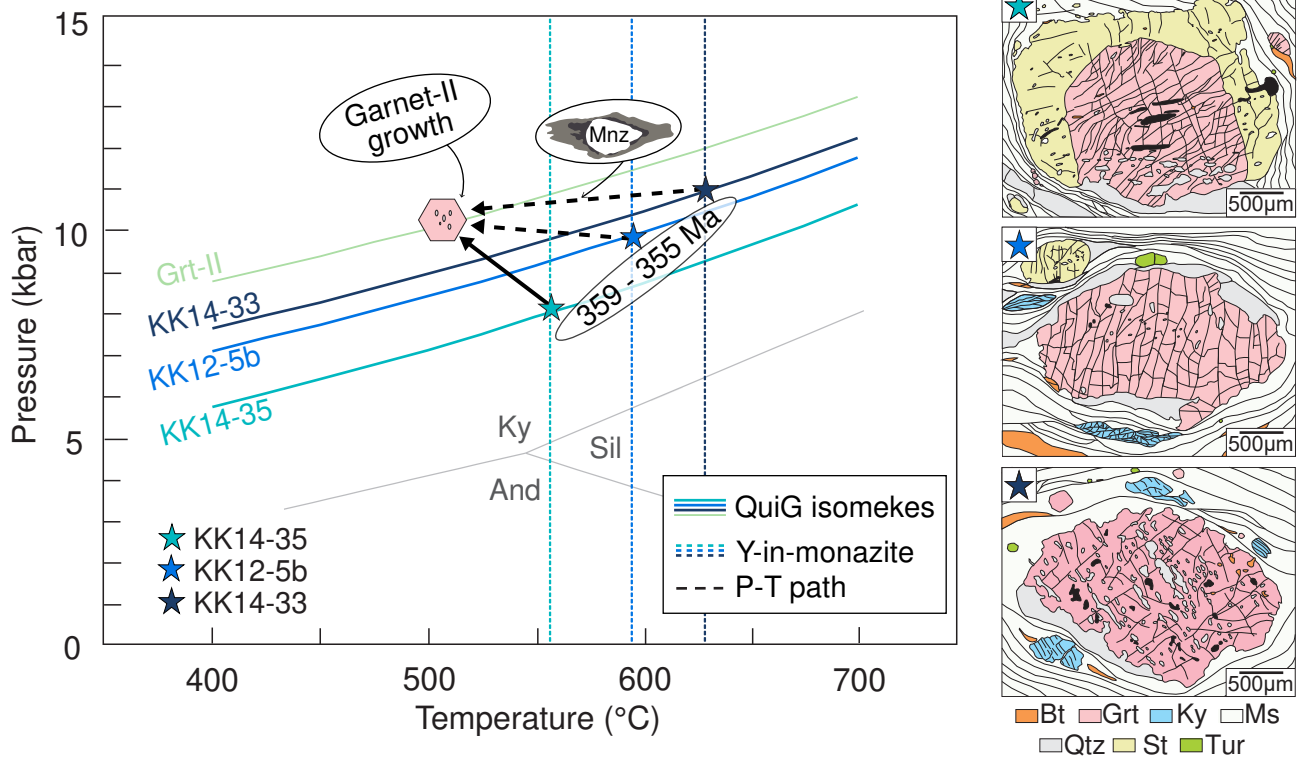


Figure 14. Pressure-temperature-time (P-T-t) evolutionary path for Pinkie unit metapelites. Quartz-in-garnet (QuiG) barometry, trace-element thermometry and the results of calculated phase equilibria are shown. The garnet nucleation PT conditions for studied samples are marked by stars. The growth of monazite during prograde metamorphism is indicated by ellipse. The breaking down of the monazite is shown by simplified sketch on the retrograde path.